




## Article

# DNA Binding and Cleavage, Stopped-Flow Kinetic, Mechanistic, and Molecular Docking Studies of Cationic Ruthenium(II) Nitrosyl Complexes Containing “NS<sub>4</sub>” Core

Hadeer A. Shereef <sup>1,2</sup>, Yasmine S. Moemen <sup>3</sup>, Fawzia I. Elshami <sup>4</sup>, Ahmed M. El-Nahas <sup>1,†</sup>, Shaban Y. Shaban <sup>4,\*</sup> and Rudi van Eldik <sup>5,6,\*</sup>

<sup>1</sup> Chemistry Department, Faculty of Science, Menoufia University, Shebin El-Kom 32512, Egypt

<sup>2</sup> Clinical Pathology Department, University Hospital, Menoufia University, Shebin El-Kom 32512, Egypt

<sup>3</sup> Clinical Pathology Department, National Liver Institute, Menoufia University, Shebin El-Kom 32512, Egypt

<sup>4</sup> Chemistry Department, Faculty of Science, Kafrelsheikh University, Kafrelsheikh 33516, Egypt

<sup>5</sup> Department of Chemistry and Pharmacy, University of Erlangen-Nuremberg, 91058 Erlangen, Germany

<sup>6</sup> Faculty of Chemistry, Nicolaus Copernicus University in Torun, 87-100 Torun, Poland

\* Correspondence: shaban.shaban@sci.kfs.edu.eg (S.Y.S.); rudi.vaneldik@fau.de (R.v.E.)

† Deceased.

## Highlights:

- Theoretical studies were performed on [RuNOTSP]<sup>+</sup>, TSPH<sub>2</sub>, and its anion TSP<sup>2-</sup> using the DFT/B3LYP method.
- Cationic complex [RuNOTSP]<sup>+</sup> and TSPH<sub>2</sub> were investigated mechanistically for ctDNA interaction.
- Spontaneous ctDNA binding via a static mechanism with two steps was reported.
- Detailed kinetic data are reported and relative reactivity is [RuNOTSP]<sup>+</sup>/TSPH<sub>2</sub> = 3/1.
- The ruthenium effect on affinity and mechanism is reported.
- The ruthenium center improves the reaction rate through coordination affinity, but does not change its mechanism.
- Molecular docking was used to predict the binding between [RuNOTSP]<sup>+</sup> and TSPH<sub>2</sub> and the receptors.
- DNA cleavage studies are correlated with kinetic data.



**Citation:** Shereef, H.A.; Moemen, Y.S.; Elshami, F.I.; El-Nahas, A.M.; Shaban, S.Y.; van Eldik, R. DNA Binding and Cleavage, Stopped-Flow Kinetic, Mechanistic, and Molecular Docking Studies of Cationic Ruthenium(II) Nitrosyl Complexes Containing “NS<sub>4</sub>” Core. *Molecules* **2023**, *28*, 3028. <https://doi.org/10.3390/molecules28073028>

Academic Editors: Girolamo Casella and Silvia Carlotto

Received: 17 January 2023

Revised: 24 March 2023

Accepted: 24 March 2023

Published: 28 March 2023



**Copyright:** © 2023 by the authors. Licensee MDPI, Basel, Switzerland. This article is an open access article distributed under the terms and conditions of the Creative Commons Attribution (CC BY) license (<https://creativecommons.org/licenses/by/4.0/>).

**Abstract:** This work aimed to evaluate in vitro DNA binding mechanistically of cationic nitrosyl ruthenium complex [RuNOTSP]<sup>+</sup> and its ligand (TSPH<sub>2</sub>) in detail, correlate the findings with cleavage activity, and draw conclusions about the impact of the metal center. Theoretical studies were performed for [RuNOTSP]<sup>+</sup>, TSPH<sub>2</sub>, and its anion TSP<sup>2-</sup> using DFT/B3LYP theory to calculate optimized energy, binding energy, and chemical reactivity. Since nearly all medications function by attaching to a particular protein or DNA, the in vitro calf thymus DNA (ctDNA) binding studies of [RuNOTSP]<sup>+</sup> and TSPH<sub>2</sub> with ctDNA were examined mechanistically using a variety of biophysical techniques. Fluorescence experiments showed that both compounds effectively bind to ctDNA through intercalative/electrostatic interactions via the DNA helix’s phosphate backbone. The intrinsic binding constants (K<sub>b</sub>), (2.4 ± 0.2) × 10<sup>5</sup> M<sup>-1</sup> ([RuNOTSP]<sup>+</sup>) and (1.9 ± 0.3) × 10<sup>5</sup> M<sup>-1</sup> (TSPH<sub>2</sub>), as well as the enhancement dynamic constants (K<sub>D</sub>), (3.3 ± 0.3) × 10<sup>4</sup> M<sup>-1</sup> ([RuNOTSP]<sup>+</sup>) and (2.6 ± 0.2) × 10<sup>4</sup> M<sup>-1</sup> (TSPH<sub>2</sub>), reveal that [RuNOTSP]<sup>+</sup> has a greater binding propensity for DNA compared to TSPH<sub>2</sub>. Stopped-flow investigations showed that both [RuNOTSP]<sup>+</sup> and TSPH<sub>2</sub> bind through two reversible steps: a fast second-order binding, followed by a slow first-order isomerization reaction via a static quenching mechanism. For the first and second steps of [RuNOTSP]<sup>+</sup> and TSPH<sub>2</sub>, the detailed binding parameters were established. The total binding constants for [RuNOTSP]<sup>+</sup> (K<sub>a</sub> = 43.7 M<sup>-1</sup>, K<sub>d</sub> = 2.3 × 10<sup>-2</sup> M<sup>-1</sup>, ΔG<sup>0</sup> = -36.6 kJ mol<sup>-1</sup>) and TSPH<sub>2</sub> (K<sub>a</sub> = 15.1 M<sup>-1</sup>, K<sub>d</sub> = 66 × 10<sup>-2</sup> M, ΔG<sup>0</sup> = -19 kJ mol<sup>-1</sup>) revealed that the relative reactivity is approximately ([RuNOTSP]<sup>+</sup>)/(TSPH<sub>2</sub>) = 3/1. The significantly negative ΔG<sup>0</sup> values are consistent with a spontaneous binding reaction to both [RuNOTSP]<sup>+</sup> and TSPH<sub>2</sub>, with the former being very favorable. The findings showed that the Ru(II) center had an effect on the reaction rate but not on the mechanism

and that the cationic  $[\text{RuNOTSP}]^+$  was a more highly effective DNA binder than the ligand  $\text{TSPH}_2$  via strong electrostatic interaction with the phosphate end of DNA. Because of its higher DNA binding affinity, cationic  $[\text{RuNOTSP}]^+$  demonstrated higher cleavage efficiency towards the minor groove of pBR322 DNA via the hydrolytic pathway than  $\text{TSPH}_2$ , revealing the synergy effect of  $\text{TSPH}_2$  in the form of the complex. Furthermore, the mode of interaction of both compounds with ctDNA has also been supported by molecular docking.

**Keywords:** DNA; ruthenium nitrosyl complexes; reaction mechanism; binding interaction; molecular docking; kinetic investigation

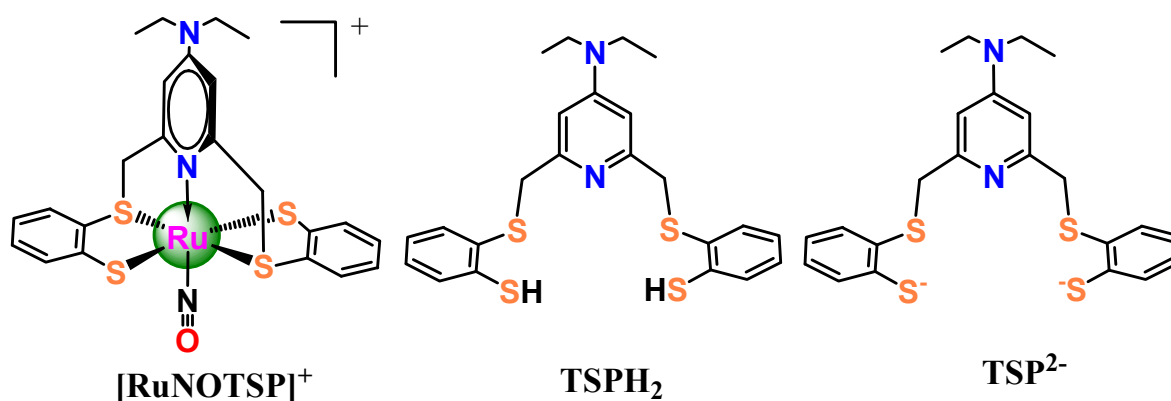
## 1. Introduction

One of the most important factors in the advancement of medicinal inorganic chemistry is still the widespread use of cisplatin and other platinum-based metallodrugs as chemotherapeutic agents against various cancers, including those of the ovary, bladder, and testicles [1–4]. In the search for coordination compounds that are toxic-free compared to cisplatin and effective against tumors, ruthenium compounds show the most promise due to their biological properties, which differ greatly from those of traditional platinum compounds in terms of their mechanism of action, toxicity, and biodistribution, and some ruthenium compounds have been shown to be quite selective for cancer cells [5–8]. It is widely known that ruthenium complexes have a strong affinity for cancer tissues and a reduced general toxicity when they bind to biological molecules such as DNA, making them potential candidates for anticancer drugs [9–16]. This is thought to be caused by ruthenium's capabilities to mimic iron when binding to biomolecules. Ruthenium-based medications may reach cancer cells more effectively because cancer cells overexpress transferrin receptors to meet their increased need for iron [17].

Few ruthenium complexes have so far been demonstrated to exhibit potential anticancer activities and have been registered in clinical trials [18,19]. These complexes have some advantages over cisplatin, such as their efficacy against cancer cell lines that are resistant to cisplatin and their higher selectivity for cancer cells compared to normal cells, which can lessen side effects [20–23]. Additionally, ruthenium complex structures may have stronger anticancer activity if biomolecules such as NO are added to them. It has been demonstrated that NO functions as a mediator in one tumor-induced angiogenic process, which is a critical step in the formation of metastasis [24–26]. The significance of ruthenium nitrosyl complexes in terms of biology, environment, and novel reactivity has been thoroughly investigated over time [27–30]. When cationic nitrosyl ruthenium complexes with multi-dentate sulfur ligands are prepared, a variety of complexes with different structures, electronic characteristics, and reactivity trails are created [31–34]. One of these cationic nitrosyl ruthenium complexes,  $[\text{RuNOTSP}]^+$  ( $\text{TSP}^{2-} = 4\text{-(diethylamino)-2,6-bis[2-mercaptophenyl]thiomethyl-pyridine(2-)}$ ), exhibits high activity against cancer cells and is resistant to air oxidation [31].

Because DNA is the primary target of most antitumor agents, the interaction of well-tailored metal complexes with DNA determines the potential of these complexes to act as potent chemotherapeutic agents. DNA is a polyelectrolyte with a high negative charge at physiological pH, and the structure of DNA is governed by electrostatic and hydrophobic interactions between the various residues in the polynucleotide chain [35]. Cationic agents are expected to bind more strongly to DNA, a negatively charged molecule, through a combination of electrostatic attraction, groove binding, and intercalation. Because cationic ruthenium complexes, among other cationic agents, have unique properties such as binding to DNA or protein [36], good luminescent behavior, and singlet oxygen-generating abilities [35], the emphasis has shifted to cationic complexes as complexing agents with DNA. In an effort to comprehend how biomolecules bind *in vitro* and determine whether the metal center is necessary for binding, the BSA binding characteristics of  $[\text{RuNOTSP}]^+$

and its ligand TSPH<sub>2</sub> have recently been reported [37] (Scheme 1). In the current study, we used cationic [RuNOTSP]<sup>+</sup> and TSPH<sub>2</sub> for DNA binding and DNA cleavage behavior to understand the action mechanism of drugs to DNA, which improves the design of drugs that target cellular DNA, in order to learn more about the anticancer activity of ruthenium complexes. This was thoroughly studied using fluorescence spectroscopy, electronic absorption spectroscopy, and gel electrophoresis to show how [RuNOTSP]<sup>+</sup> and TSPH<sub>2</sub> interact with DNA as drugs. Molecular docking was used to theoretically investigate the binding mode of [RuNOTSP]<sup>+</sup> and its ligand TSPH<sub>2</sub> for DNA binding sites. We also performed a kinetic analysis of the interaction between ctDNA-[RuNOTSP]<sup>+</sup> and ctDNA-TSPH<sub>2</sub>. In this respect, gene transport is also greatly influenced by the kinetics of DNA condensation. As it is expected that the drug interaction will happen so quickly, a fast kinetic method is needed to find transient intermediates in the interaction pathway. We employed the stopped-flow technique in earlier studies [37–41], in which sample and reagent solutions were quickly mixed, and measurements were taken almost immediately after mixing. Using this technique, it was found that other factors, such as drug affinity and the kinetic stability of the DNA/protein–drug complex, are also essential for biological activity when examining how various drugs interacted with DNA and proteins. In this study, we evaluated the compound–DNA affinity using the stopped-flow method. We also examined the kinetic stability and, finally, proposed an interaction mechanism. The geometrically optimized parameters (bond lengths, bond angles, and dihedral angles) were computed using DFT/B3LYP theory to conduct computational studies on the cationic component [RuNOTSP]<sup>+</sup>, TSPH<sub>2</sub>, and its anion TSP<sup>2-</sup>.



**Scheme 1.** Structure of [RuNOTSP]<sup>+</sup>, TSPH<sub>2</sub>, and its anion TSP<sup>2-</sup>, respectively.

## 2. Results and Discussion

Ruthenium nitrosyl complex [RuNOTSP]Br was prepared in our lab according to the methods described [33]. Starting from 4-diethylamino-2,6-bis(hydroxymethyl)pyridine, the final product 4-diethylamino-2,6-bis(bromomethyl)pyridine was obtained. The latter was added to a solution of NBu<sub>4</sub>[Ru(NO)(S<sub>2</sub>C<sub>6</sub>H<sub>4</sub>)<sub>2</sub>] in boiling THF, giving a brown suspension, from which a brown solid of [RuNOTSP]Br was isolated by filtration. It could be isolated in an analytically pure form, proved soluble in MeOH, CH<sub>2</sub>Cl<sub>2</sub>, and DMF, and its elemental analyses and spectroscopic data (IR, <sup>1</sup>H, <sup>13</sup>C NMR, mass spectra) were compatible with those reported. [RuNOTSP]Br is easily hydrolyzed by concentrated hydrochloric acid in CH<sub>2</sub>Cl<sub>2</sub> at room temperature, yielding the ligand as the pyridinium salt TSPH<sub>2</sub> HCl (Scheme S1). The (NO) wave number of complex [RuNOTSP]Br is 1858 cm<sup>-1</sup> in KBr, 1870 cm<sup>-1</sup> in THF, and 1880 cm<sup>-1</sup> in MeOH. UV–vis spectra in methanol revealed that [RuNOTSP]<sup>+</sup> is stable over time, with no discernible changes. This indicates that under these conditions, reducing [RuNOTSP]<sup>+</sup> to [RuNOTSP] is difficult. As a result, under these conditions, nitrosyl ligand (NO<sup>+</sup>) was coordinated to the ruthenium center. Cyclic voltammetry could also help with the difficult reduction of [RuNOTSP]<sup>+</sup> to [RuNOTSP] in methanol. Within the solvent limits, the cyclic voltammogram of [RuNOTSP]<sup>+</sup> in MeOH

shows two successive reduction processes. The observed redox processes at  $E_{1/2} = \text{ca. } -467$  and  $-1524$  mV vs. NHE (Figure 1) were the most likely, as seen in the two stepwise one-electron

compared to the related complexes ( $-467, -1524$  mV vs.  $-275, -1200$  mV) imply that the  $\text{Et}_2\text{N}$  substituent makes the  $[\text{RuNOTSP}]^+$  fragment more difficult for reduction. This result is consistent with the differences in (NO) frequencies (KBr) of  $[\text{RuNOTSP}]^+$  ( $1858\text{ cm}^{-1}$ ) in comparison to the previously reported complex ( $1892\text{ cm}^{-1}$ ) [42].

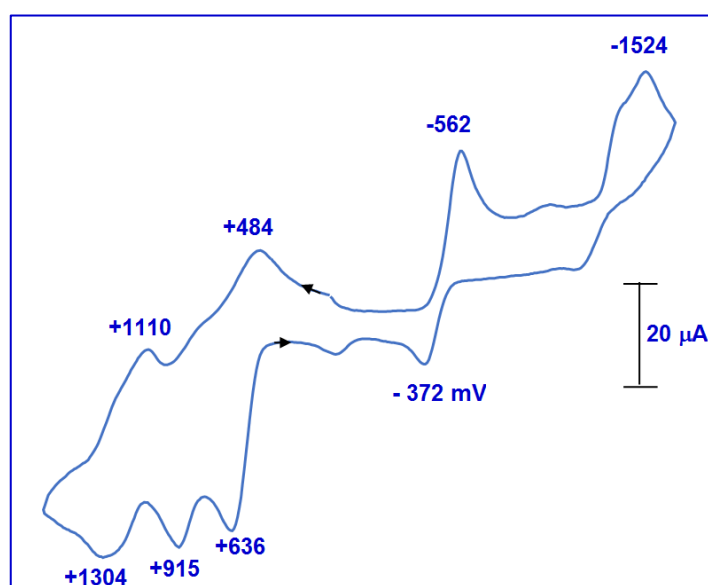
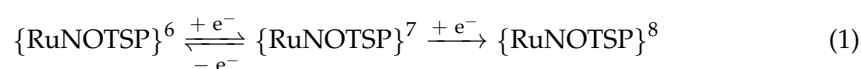
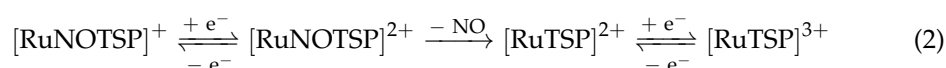


**Figure 1.** Cyclic voltammogram of  $[\text{RuNOTSP}]\text{Br}$  in  $\text{MeOH}$  ( $10^{-3}$  M,  $10^{-1}$  M  $\text{NBu}_4\text{PF}_6$ ,  $v = 50$  mV/s).

Three oxidation processes were observed in the anodic region at  $E_{1/2} = \text{ca. } +560, +915,$  and  $+1207$  mV, which could be tentatively assigned to the three stepwise one-electron oxidations designated in Equation (2).



### 2.1. Computational Findings

Figure 2 depicts the optimized geometries of the investigated  $\text{TSPH}_2$ ,  $\text{TSP}^{2-}$  anion, and  $[\text{RuNOTSP}]^+$ . These calculations reveal that  $\text{TSPH}_2$  has a square-pyramidal structure and pseudo-octahedral overall geometry around the metal center. The two thioether and two thiolate donor atoms of the  $\text{TSPH}_2$  ligand occupy the corresponding trans position and provide the steric rigidity of the  $\text{py}(\text{CH}_2)_2$  backbone, as does the bridging S-donor and  $\text{TSPH}_2$  or the pyridine N-donor of the metal fragment.

To shed light on the electronic structures of  $\text{TSPH}_2$ ,  $\text{TSP}^{2-}$  anion, and  $[\text{RuNOTSP}]^+$ , the natural population analysis (NPA) was carried out [43–45]. Atomic numbering along with the data are listed in the Supplementary Materials. Table 1 shows charges from natural population analysis over some selected atoms. The negative charge on the thiolate sulfur atoms of  $\text{TSP}^{2-}$  anion (S38,  $-0.477$  and S48,  $-0.477$ ) is larger than that for the neutral ligand  $\text{TSPH}_2$  (S38,  $0.066$  and S48,  $0.066$ ), whereas both are larger than that of the cationic complex  $[\text{RuNOTSP}]^+$  (S12,  $0.121$  and S24,  $0.1563$ ). This indicates that the two negative charges on the thiolate of  $\text{TSP}^{2-}$  are shifted towards the ruthenium center after complexation. The same trend is also valid for the thioether sulfur atoms of  $\text{TSP}^{2-}$  anion (S10, S26),  $\text{TSPH}_2$  (S10, S26), and cationic complex  $[\text{RuNOTSP}]^+$  (S11, S23). So, the charge density on the

thiolate and thioether sulfur atoms is delocalized over the ruthenium center and makes the ruthenium center more negative (Ru,  $-0.674$ ). The charge density on the pyridine nitrogen atom (N26,  $-0.43862$ ) is more negative compared to that of the nitrogen atom of the nitrosyl group, which indicates that the positive charge on the complex is more concentrated in the nitrosyl group.

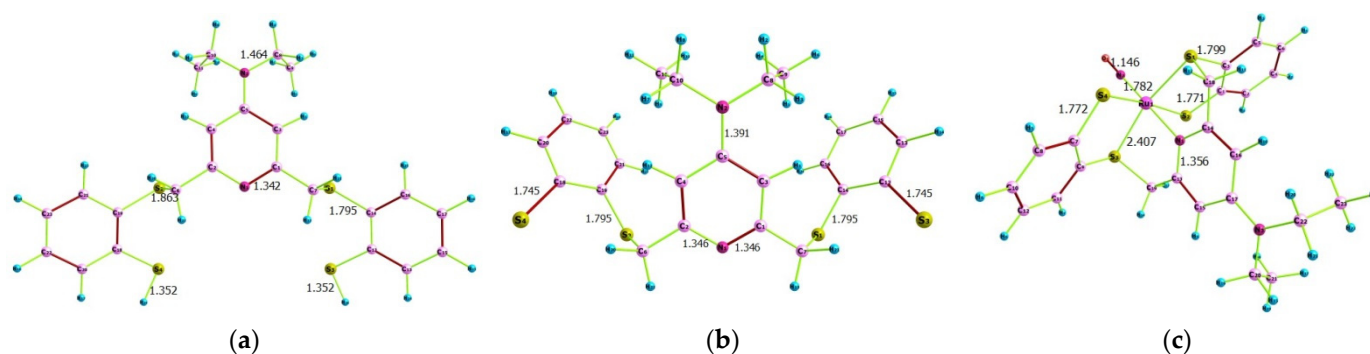


**Figure 2.** Computational optimized geometries: (a) TSPH<sub>2</sub>, (b) TSP<sup>2-</sup>-anion, and (c) [RuNOTSP]<sup>+</sup>.

**Table 1.** NBA charges of selected atoms of TSPH<sub>2</sub>, TSP<sup>2-</sup> anion, and [RuNOTSP]<sup>+</sup> at B3LYP/3-21G(d).

Atom (No)	TSPH <sub>2</sub>	TSP <sup>2-</sup>	Atom (No)	[RuNOTSP] <sup>+</sup>
S (10)	0.23735	0.21314	S (11)	0.68887
S (26)	0.23736	0.21314	S (23)	0.69449
S (38)	0.06633	$-0.47654$	S (12)	0.12102
S (48)	0.06634	$-0.47655$	S (24)	0.15628
N (1)	$-0.48666$	$-0.51020$	N (26)	$-0.43862$
N (11)	$-0.44178$	$-0.45570$	N (42)	$-0.40769$
	-	-	N (35)	0.45495
	-	-	Ru	$-0.67395$

### 2.1.1. Quantum Chemical Parameters

In a complex formation system, the ligand serves as an electron donor (Lewis base), and the metal ion serves as an electron acceptor (Lewis acid). A ligand with the correct softness value usually chelates metal ions successfully [46]. Additionally, the chemical reactivity, stability, and hardness of the compounds are explained by the energy difference between HOMO and LUMO. A hard molecule is one with a large HOMO-LUMO gap, whereas a soft molecule is one with a small HOMO-LUMO gap. While softness gauges chemical reactivity, hardness gauges molecule stability. From the data of HOMO and LUMO energies, the energy gap ( $\Delta E$ ), absolute electronegativity ( $\chi$ ), absolute hardness ( $\eta$ ), electronic chemical potentials ( $P_i$ ), absolute softness ( $\sigma$ ), global softness ( $S$ ), and global electrophilicity ( $\omega$ ) are listed in Table 2. The comparative investigation clarifies the following points in association with TSPH<sub>2</sub>: (i) the soft character of TSPH<sub>2</sub> shows its flexible reactivity toward the metal ions; (ii)  $\chi$  is positive whereas  $P_i$  is negative values indicated that the molecule is able to capture electrons from its environment and its energy must decrease when accepting the electron charge. The quantum chemical parameters for [RuNOTSP]<sup>+</sup> elicit the following points: (i) the energy gaps of the cation [RuNOTSP]<sup>+</sup> in comparison with TSPH<sub>2</sub> reflect the high softness and biological activity of metal complexes than TSPH<sub>2</sub>; (ii)  $E_{\text{HOMO}}$  increase and  $E_{\text{LUMO}}$  more than TSPH<sub>2</sub>, which might be related to the strength of metallic bonds.

**Table 2.** Quantum parameters for TSP-H<sub>2</sub>; TSP<sup>2-</sup>, anion and [RuNOTSP]<sup>+</sup>.

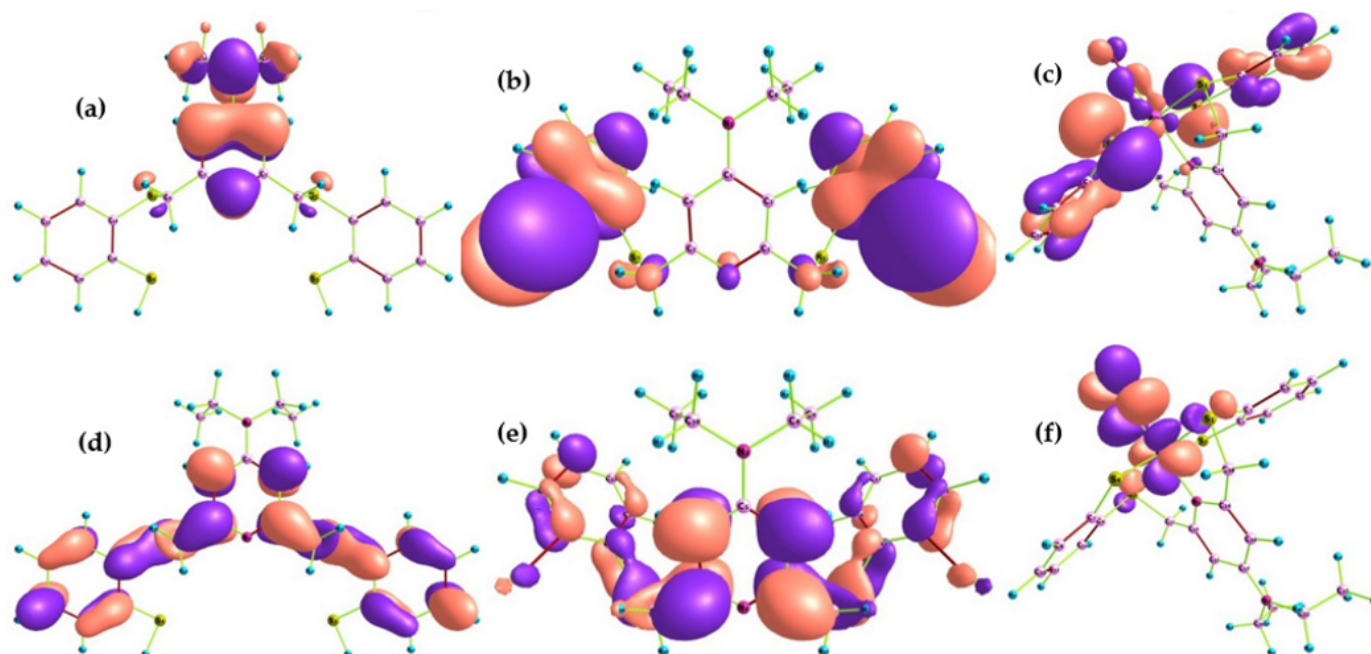
Parameter	TSPH <sub>2</sub>	TSP <sup>2-</sup>	[RuNOTSP] <sup>+</sup>
$E_{\text{HOMO}}$ (eV)	$-5.56$	1.04	$-8.09$
$E_{\text{LUMO}}$ (eV)	$-0.72$	4.70	$-5.87$

Table 2. Cont.

Parameter	TSPH <sub>2</sub>	TSP <sup>2-</sup>	[RuNOTSP] <sup>+</sup>
E <sub>LUMO</sub> – E <sub>HOMO</sub> (eV)	4.84	3.66	2.22
χ (eV)	3.14	–2.87	6.98
η (eV)	2.421	1.831	1.110
Π (eV)	–3.14	2.87	–6.98
σ (eV <sup>-1</sup> )	0.413	0.456	0.901
S (eV <sup>-1</sup> )	0.206	0.273	0.451
ω (eV)	2.037	2.249	21.946

### 2.1.2. Frontier Molecular Orbitals and Chemical Reactivity

Frontier molecular orbitals (FMOs) are used to understand several types of reactions and explain the interaction between the ligand and the metal ion, besides predicting the most reactive position in the molecules and their properties. The HOMO level is the highest energy orbital containing electrons that act as an electron donor, while the LUMO is the lowest energy orbital that acts as an electron acceptor. The calculated HOMO of TSPH<sub>2</sub> is located on C<sub>3</sub>, C<sub>4</sub>, C<sub>5</sub>, C<sub>6</sub>, C<sub>8</sub>, C<sub>9</sub>, C<sub>10</sub>, C<sub>11</sub>, N<sub>1</sub>, N<sub>2</sub>, S<sub>1</sub>, and S<sub>2</sub>, whereas the HOMO of the TSP<sup>2-</sup> anion spreads over two benzene rings, N<sub>1</sub>, S<sub>1</sub>, S<sub>2</sub>, S<sub>3</sub>, and S<sub>4</sub>. The LUMO of TSPH<sub>2</sub> and TSP<sup>2-</sup> anion is distributed over the whole skeleton, as shown in Figure 3. These orbitals over the relevant centers indicate the sites that can act as an electron donor in TSPH<sub>2</sub> when coming near the metal ion and those that can accept the electron via back donation from the metal ion to form stable complexes. Deprotonation of the thiol groups further adds new centers that share HOMO orbitals that become ready for binding with interacting metal ions. The HOMO level of [RuNOTSP]<sup>+</sup> spreads over two benzene rings, Ru, N<sub>3</sub>, O<sub>1</sub>, S<sub>3</sub>, and S<sub>4</sub>, whereas LUMO is located on Ru, N<sub>3</sub>, O<sub>1</sub>, S<sub>1</sub>, and S<sub>2</sub> (Figure 3).



**Figure 3.** HOMO of (a) TSPH<sub>2</sub>, (b) TSP<sup>2-</sup>, and (c) [RuNOTSP]<sup>+</sup> and LUMO of (d) TSPH<sub>2</sub>, (e) TSP<sup>2-</sup>, and (f) [RuNOTSP]<sup>+</sup>.

Molecular electrostatic potential (MEP) is a very suitable tool for highlighting reactive sites towards electrophilic and nucleophilic attack and also determines the relative polarity of molecules. The MEPs of TSPH<sub>2</sub> and [RuNOTSP]<sup>+</sup> are presented in Figure 4. The red and yellow sites (negative regions) of MEP are related to electrophilic reactivity, while the blue and green sites (positive regions) are related to nucleophilic reactivity. Figure 4 reveals

that the negative MEP regions of TSPH<sub>2</sub> are concentrated on the pyridine nitrogen atom and sulfur atoms, thus confirming their electron donor ability.

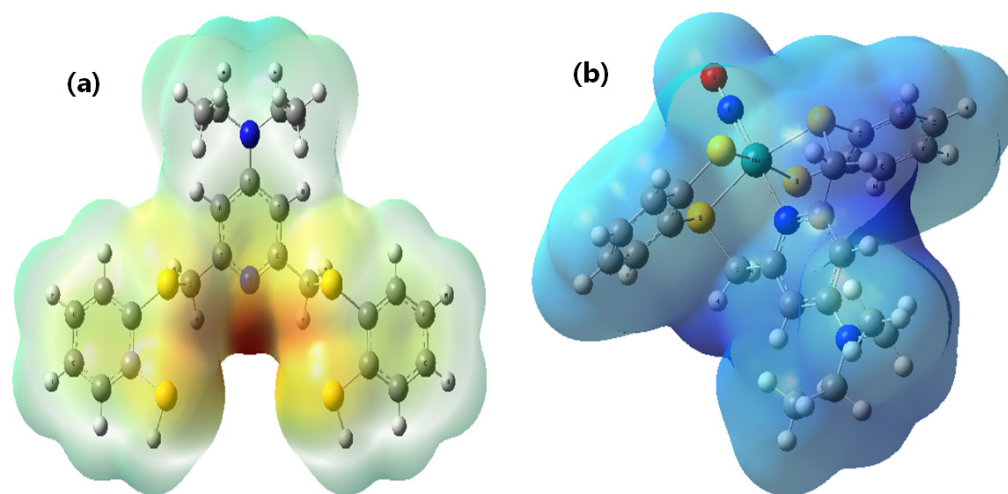


**Figure 4.** Molecular electrostatic potential of (a) TSPH<sub>2</sub> and (b) [RuNOTSP]<sup>+</sup>.

## 2.2. DNA Interaction Studies

### 2.2.1. Fluorescence Spectroscopy

The most accurate and sensitive method for characterizing how drugs interact with CT-DNA is fluorescence emission spectra [47,48]. Both [RuNOTSP]<sup>+</sup> and TSPH<sub>2</sub> exhibit a noticeable increase in emission when CT-DNA is added because they are both luminescent in the absence of DNA. Figure 5 demonstrates that increasing the concentration of DNA at 25 °C and pH = 7.2 resulted in a regular increase in the fluorescence intensity of both compounds without shifting the fluorescence emission maximum. With increasing DNA concentration, [RuNOTSP]<sup>+</sup> and TSPH<sub>2</sub> solution's maximum fluorescence intensity increases steadily at 303 nm, with no discernible change in the position or shape of the emission bands. The increase in emission intensity is most likely caused by the modification of the compound's environment and the degree to which the compound has been inserted into the hydrophobic environment inside the DNA helix. Fewer solvent molecules can reach the binding site due to the hydrophobic environment inside the DNA helix, preventing the quenching effect. The DNA helix effectively protected both compounds, as evidenced by the fact that relaxation vibrations decreased and emission intensity increased. The increase in emission intensities reveals their binding to DNA into its hydrophobic pocket along the major and minor grooves [49,50]. These fluorescence improvements demonstrate that [RuNOTSP]<sup>+</sup> and TSPH<sub>2</sub> both interacted with DNA to increase the quantum efficiency of the complex. Similar to the quenching process, Equation (3) can be used to determine the enhancement constant [51,52]:

$$I_0/I = 1 - K_E[E] \quad (3)$$

Equation (3) can be written in the case that a dynamic process contributes to the enhancing mechanism, as follows (Equation (4)):

$$I_0/I = 1 - K_D[E] = 1 - k_B \tau_0[E] \quad (4)$$

where  $k_D$  is the dynamic enhancement constant (similar to a dynamic quenching constant),  $k_B$  is the bimolecular enhancement constant (similar to a bimolecular quenching constant), and  $\tau_0$  is the lifetime of the fluorophore in the absence of the enhancer, which equals about  $10^{-9}$  s [53], and  $[E]$  is the concentration of enhancer. The plot of  $I_0/I$  vs.  $[E]$ , which gives the  $K_D$  values by slope, and the values of  $k_B$  are calculated by using Equation (4), and these results are given in Figure 6a and summarized in Table 3. The plots exhibited a linear relationship, which indicated only one type of enhancing (static or dynamic

enhancing). The dynamic constant ( $K_D$ ) of  $[\text{RuNOTSP}]^+$  ( $3.3 \pm 0.3 \times 10^4 \text{ M}^{-1}$ ) is higher than that of its ligand  $\text{TSPH}_2$  ( $2.6 \pm 0.2 \times 10^4 \text{ M}^{-1}$ ). The enhancement rate constant of the biomolecule ( $k_B$ ) of  $[\text{RuNOTSP}]^+$  and  $\text{TSPH}_2$  is calculated as  $(3.3 \pm 0.3) \times 10^{12}$  and  $(2.6 \pm 0.2) \times 10^{12} \text{ L}\cdot\text{mol}^{-1}\cdot\text{s}^{-1}$  at 298 K, respectively. When the equivalence of the bimolecular quenching and enhancement constants are considered, the latter is found to be greater than the maximum possible value ( $1 \times 10^{10} \text{ L}\cdot\text{mol}^{-1}\cdot\text{s}^{-1}$ ) in aqueous medium. Thus, the fluorescence enhancement is not initiated by a dynamic process; rather, a static process involving complex formation in the ground state is proposed, and the fluorescence enhancement is controlled by a static process [50,51]. The calculated association constants for the ctDNA- $\text{TSPH}_2$  and ctDNA- $[\text{RuNOTSP}]^+$  adducts indicate high-affinity  $\text{TSPH}_2$ - and  $[\text{RuNOTSP}]^+$ -polynucleotide binding.

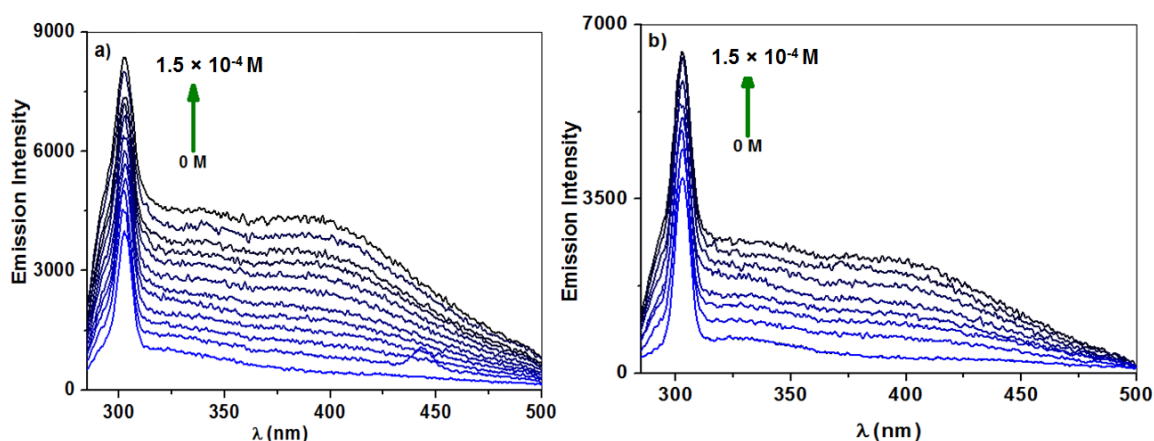


**Figure 5.** Luminescence spectra of (a)  $[\text{RuNOTSP}]^+$  and (b)  $\text{TSPH}_2$  after adding ctDNA system.  $T = 298 \text{ K}$ ,  $\lambda_{\text{exc}} = 284 \text{ nm}$ ,  $\lambda_{\text{em}} = 303 \text{ nm}$ ,  $\text{pH} = 7.2$ .

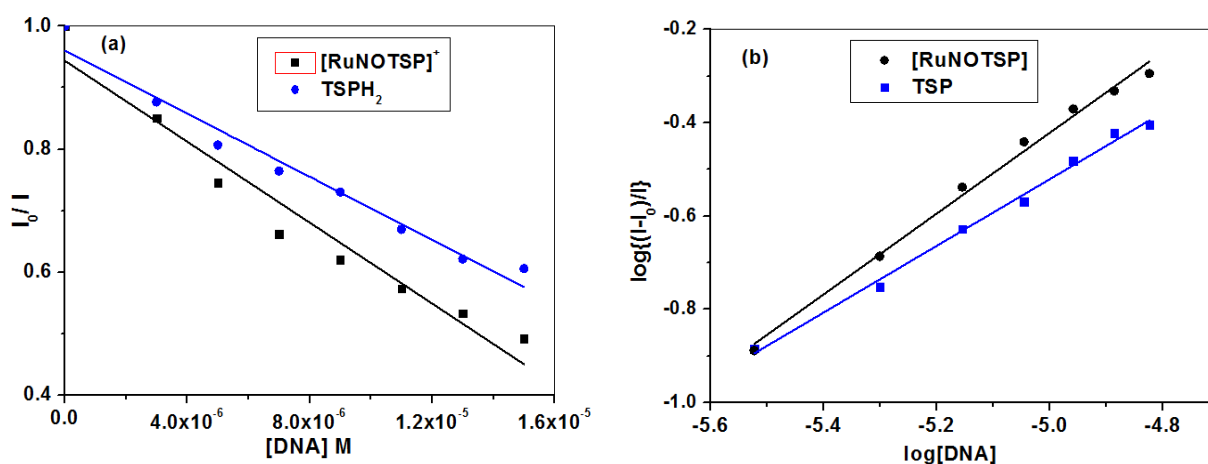


**Figure 6.** (a) Stern–Volmer plot for the observed fluorescence enhancement of  $[\text{RuNOTSP}]^+$  and  $\text{TSPH}_2$  upon addition of ctDNA; (b) plot of  $\log((I - I_0)/I)$  vs.  $\log[\text{DNA}]$ .

**Table 3.** Dynamic enhancement, bimolecular enhancement, formation constants, and number of binding sites of the complex by the reaction of  $[\text{RuNOTSP}]^+$  and  $\text{TSPH}_2$  with CT-DNA.

Compound	$K_D$ ( $\text{L mol}^{-1}$ )	$K_B$ ( $\text{L mol}^{-1} \text{ s}^{-1}$ )	n	$K_f$
$[\text{RuNOTSP}]^+$	$(3.3 \pm 0.3) \times 10^4$	$(3.3 \pm 0.3) \times 10^{12}$	0.9	$(0.81 \pm 0.01) \times 10^4$
$\text{TSPH}_2$	$(2.6 \pm 0.2) \times 10^4$	$(2.6 \pm 0.2) \times 10^{12}$	0.7	$(0.13 \pm 0.10) \times 10^4$



### 2.2.2. Equilibrium Binding Titration

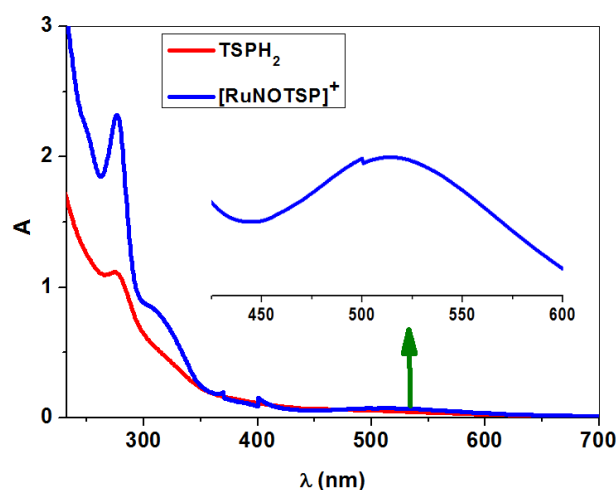
The following Equation (5) was used to determine the binding constant ( $K_f$ ) and the number of  $[\text{RuNOTSP}]^+$  and  $\text{TSPH}_2$  molecules bound per polynucleotides ( $n$ ) for the complex formation between both compounds and DNA [54]:

$$\log\left(\frac{I_0 - I}{I}\right) = \log K_f + n \log[\text{DNA}] \quad (5)$$

where  $I_0$  and  $I$  are the fluorescence intensity of the fluorophore in the absence and presence of different concentrations of DNA, respectively. The linear equations of  $\log(I - I_0)/I$  vs.  $\log[\text{DNA}]$  are shown in Figure 6b. The  $K_f$  values demonstrate the complex's remarkably high affinity for DNA, and the  $n$  values from the slope of the straight line are 0.9 and 0.7 for ctDNA- $[\text{RuNOTSP}]^+$  and ctDNA- $\text{TSPH}_2$  adducts, respectively.

### 2.2.3. UV-Vis Spectroscopy

One of the most effective methods for studying DNA binding is electronic absorption spectroscopy [55]. The  $\pi$ - $\pi^*$  transitions of DNA bases are what cause the DNA band to appear at 260 nm. Changes in the stacking pattern, dissolution of the hydrogen bonds between complementary strands, covalent binding of DNA bases, and intercalative mode, which involves a strong stacking interaction between aromatic rings of molecules and the base pairs of DNA, are the causes of the hypochromism, red, and/or blue shifts of this band [56,57]. In Tris buffer, the electronic spectrum of  $\text{TSPH}_2$  is characterized by an intense ligand-centered transition in the UV region at 276 nm, which is blue shifted in  $[\text{RuNOTSP}]^+$  and appears at 272 nm. This ultraviolet band can be attributed to  $\pi$ - $\pi^*$  transition. Furthermore, a metal-to-ligand charge transfer (MLCT) in the visible region at 310 nm for  $[\text{RuNOTSP}]^+$  was observed, which was attributed to the overlap of  $\text{Ru}(d_\pi)$ -TSP ( $\pi^*$ ).  $[\text{RuNOTSP}]^+$  exhibited a visible band at 514 nm that can be attributed to the d-d transition (Figure 7).



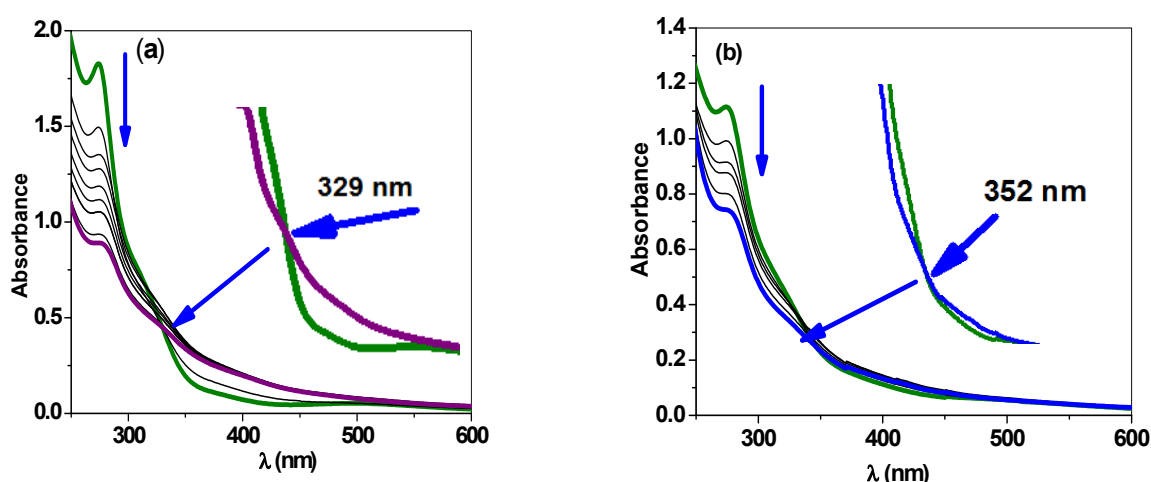
**Figure 7.** UV-vis absorption spectra of  $[\text{RuNOTSP}]^+$  and  $\text{TSPH}_2$  in methanol.

Figure 8 shows the absorption spectra of  $[\text{RuNOTSP}]^+$  and  $\text{TSPH}_2$  in the absence and presence of increasing amounts of CT-DNA. The UV-vis absorption of  $[\text{RuNOTSP}]^+$  and  $\text{TSPH}_2$  is significantly perturbed by the addition of increasing amounts of CT-DNA. In detail, the UV absorption bands of  $[\text{RuNOTSP}]^+$  (272 nm) and  $\text{TSPH}_2$  (276 nm) show a red shift of about 3 nm and hypochromism (Figure 8). For  $[\text{RuNOTSP}]^+$ , a clear isosbestic point was observed at 329 nm, whereas for  $\text{TSPH}_2$ , the isosbestic point comes at 352 nm (Figure 8). Similar spectral properties, such as bathochromic shift and hypochromism in the presence of CT-DNA, have been observed for ruthenium (II) complexes and have been linked to a mode of binding involving an interaction of aromatic chromophores with the base pairs of ctDNA that stacks [58]. Using Equation (6) [59] and Figure 9, it was discovered that

[RuNOTSP]<sup>+</sup> and TSPH<sub>2</sub> have intrinsic binding constants,  $K_b$ , of  $(2.4 \pm 0.2) \times 10^5 \text{ M}^{-1}$  and  $(1.9 \pm 0.3) \times 10^5 \text{ M}^{-1}$ , respectively. These values are higher than those reported by Barton and colleagues [60] for related ruthenium complexes ( $1.15 \times 10^4 \text{ M}^{-1}$ ). Furthermore, the  $K_b$  values are very close to the binding constants of the delta and lambda isomers of [Ru(*o*-phen)<sub>3</sub>]<sup>2+</sup>, which were assigned as non-intercalators [61]. This result indicated that [RuNOTSP]<sup>+</sup> binds to DNA stronger than TSPH<sub>2</sub>.

$$\frac{1}{A_{\text{obs}} - A_0} = \frac{1}{A_c - A_0} + \frac{1}{K_b(A_c - A_0)[\text{DNA}]} \quad (6)$$

where  $A_{\text{obs}}$ ,  $A_0$ , and  $A_c$  represent the observed absorbance during the interaction, the absorbance of DNA only, and the absorbance of DNA with the compound, respectively.



**Figure 8.** UV-vis absorption spectral changes recorded during the reaction of different concentrations of DNA with (a) [RuNOTSP]<sup>+</sup>; (b) TSP-H<sub>2</sub> at 274 nm.

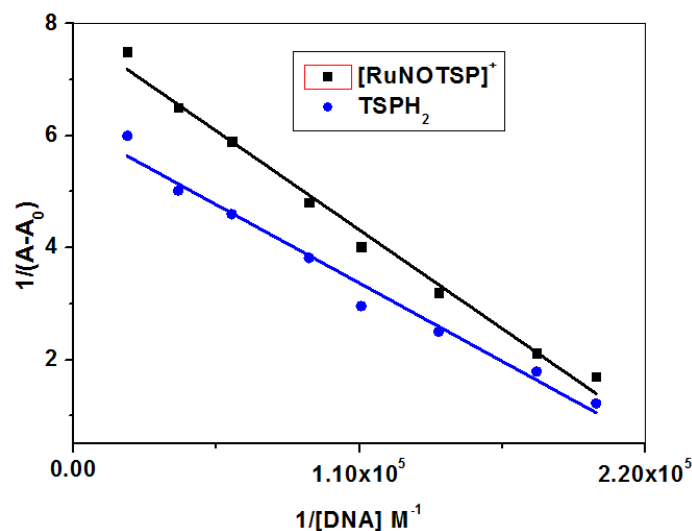


**Figure 9.** Plot of  $\frac{1}{A_{\text{obs}} - A_0}$  vs.  $\frac{1}{[\text{DNA}]}$ .

#### 2.2.4. Stopped-Flow Spectroscopic Studies and Kinetic Investigation

Any potential polycation gene delivery agent must meet two crucial requirements: (a) the capacity to completely neutralize the charge of the native DNA, resulting in a more compact state for the polycomplexes formed by DNA and polycations; and (b) the ability to dissociate the DNA-polycation complexes in the target cell's cytoplasm [62–64]. The kinetic parameters of the DNA polycomplex formation process may hold some crucial information in this regard. To keep track of the process' kinetic parameters, we used the

stopped-flow method. Figure 10 uses typical kinetic traces to show the formation of the ctDNA-[RuNOTSP]<sup>+</sup> and ctDNA-TSPH<sub>2</sub> complexes after [RuNOTSP]<sup>+</sup> and TSPH<sub>2</sub> have bound to the ctDNA in a 10 mM phosphate buffer solution. By fitting the kinetic curves to an exponential sum, we were able to analyze the multi-exponential interaction (Equation (7)).

$$A_t = a_1 e^{-k_{\text{obs}1} t_1} + a_2 e^{-k_{\text{obs}2} t_2} + A_0 \quad (7)$$

where  $A_t$  is the absorbance intensity at time  $t$ . Data analysis was performed using Origin 8.0 software. The number of exponentials was increased until there was no discernible systematic deviation of the residual. Figure 10 shows experimental plots of the absorption intensity of CTDNA-[RuNOTSP]<sup>+</sup> and ctDNA-TSPH<sub>2</sub> at 260 nm as a function of time at 25 °C for each of the two compounds. Table 4 shows the observed rate constants  $k_{\text{obs}}$  as a function of [RuNOTSP]<sup>+</sup> and TSPH<sub>2</sub> concentrations at constant DNA concentration and temperature. The average of three separate experiments serves as the rate constant. The values of these rates were at least an order of magnitude apart for all of the [RuNOTSP]<sup>+</sup> and TSPH<sub>2</sub> under study. ctDNA-[RuNOTSP]<sup>+</sup> and ctDNA-TSPH<sub>2</sub> complexes were formed via a bimolecular mechanistic pathway. From the exponential plots that followed the order  $k_1 \gg k_2$ , we were able to determine two relative rate constants ( $k_1$  and  $k_2$ ) for the binding process. All kinetic curves were able to fit into the bi-exponential function (Equation (7)), indicating the formation of complexes involved in a two-step process. The initial step is the fast step (rate constant  $k_{\text{obs}1}$ ), in which [RuNOTSP]<sup>+</sup> and TSPH<sub>2</sub> bind to ctDNA in a reversible reaction to form the binary intermediate via electrostatic interactions. The initial reaction step is thought to be the complexation and production of binary complexes. The second step (rate constant  $k_{\text{obs}2}$ ) of [RuNOTSP]<sup>+</sup> and TSPH<sub>2</sub> is slower than the first, involving compaction of the ctDNA and simultaneous internal rearrangement of the CTDNA-[RuNOTSP]<sup>+</sup> and CTDNA-TSPH<sub>2</sub> complexes [65–67].

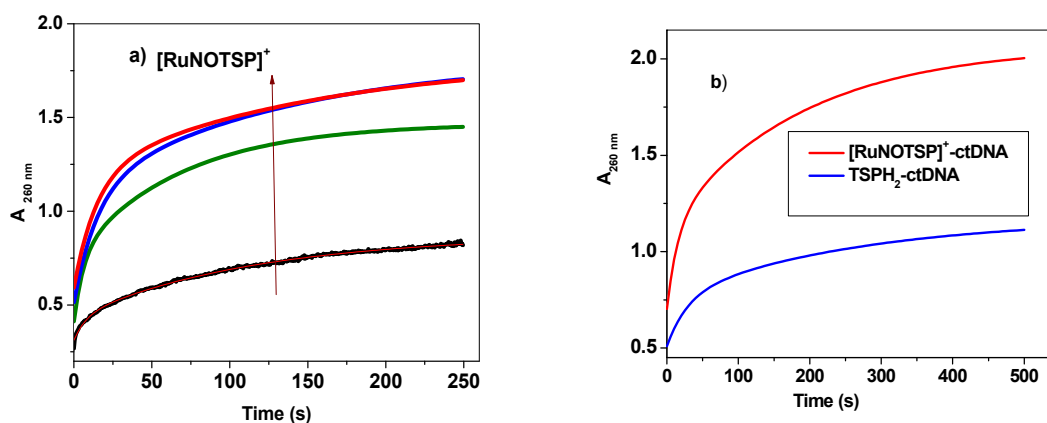


**Figure 10.** (a) Absorption intensity of the formation of ctDNA-[RuNOTSP]<sup>+</sup> complex as a function of time after mixing of ctDNA with a different concentrations of [RuNOTSP]<sup>+</sup>; (b) absorption intensity of the formation of ctDNA-TSPH<sub>2</sub> and ctDNA-[RuNOTSP]<sup>+</sup> complexes as a function of time after mixing for long time.

**Table 4.** Rate constants, affinities, and dissociation constants recorded during the reaction of DNA with [RuNOTSP]<sup>+</sup> and TSPH<sub>2</sub> at 298 K.

	Activation Parameters	[RuNOTSP] <sup>+</sup>	TSPH <sub>2</sub>
First interaction step	$k_1$ [M <sup>-1</sup> s <sup>-1</sup> ]	1.0 ± 0.2	0.7 ± 0.1
	$k_{-1}$ [10 <sup>-2</sup> s <sup>-1</sup> ]	4.1 ± 0.0	5.5 ± 0.0
	$K_{a1}$ [M <sup>-1</sup> ]	45.6	12.7
	$K_{d1}$ [10 <sup>-2</sup> M]	2.2	7.9
	$\Delta G_1^\ddagger$ [kJ mol <sup>-1</sup> ]	-17.1	-6.1

Table 4. Cont.

	Activation Parameters	[RuNOTSP] <sup>+</sup>	TSPH <sub>2</sub>
Second interaction step	K <sub>2</sub> [M <sup>-1</sup> s <sup>-1</sup> ]	0.5 ± 0.0	0.2 ± 0.1
	k <sub>-2</sub> [10 <sup>-2</sup> s <sup>-1</sup> ]	1.1 ± 0.0	0.3 ± 0.3
	K <sub>a2</sub> [M <sup>-1</sup> ]	40	59
	K <sub>d2</sub> [10 <sup>-2</sup> M]	2.5	1.69
	ΔG <sub>2</sub> <sup>#</sup> [kJ mol <sup>-1</sup> ]	-19.48	-13.17
Overall reaction data	K <sub>d</sub> [10 <sup>-2</sup> M]	2.28	66
	K <sub>a</sub> [M]	43.7	15.1
	ΔG <sup>#</sup> [kJ mol <sup>-1</sup> ]	-36.54	-19.3

Figure 11 depicts plotting of  $k_{\text{obs}1}$  vs. the concentration of [RuNOTSP]<sup>+</sup> and TSPH<sub>2</sub> and for the first step gave a linear relationship with a slope  $k_{\text{on}}$  [M<sup>-1</sup> s<sup>-1</sup>] and an intercept  $k_{\text{off}}$  [s<sup>-1</sup>], and the observed rate constant can be expressed by Equation (8).

$$k_{\text{obs}1} = k_{\text{off}} + k_{\text{on}}[\text{RuNOTSP}] \quad (8)$$

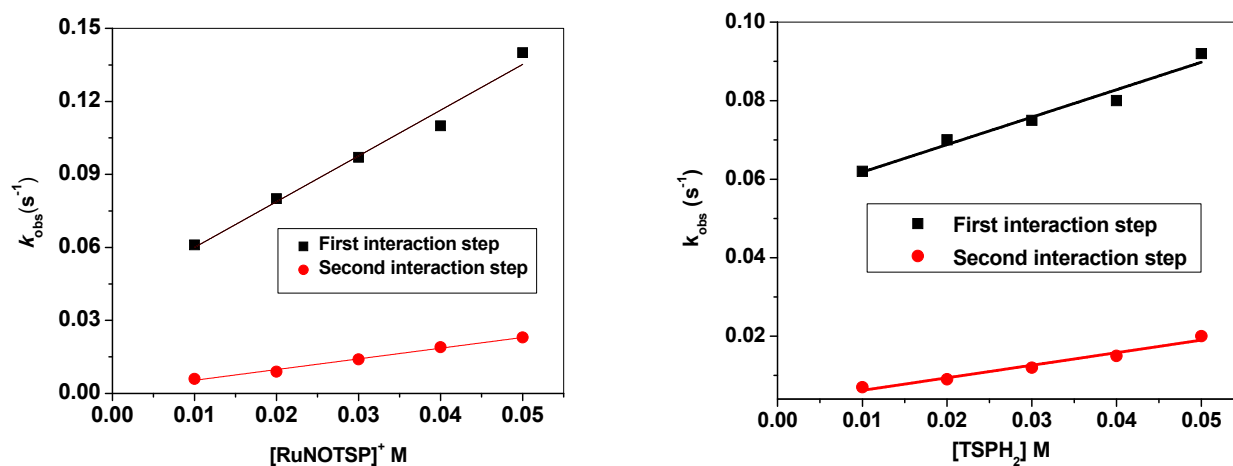
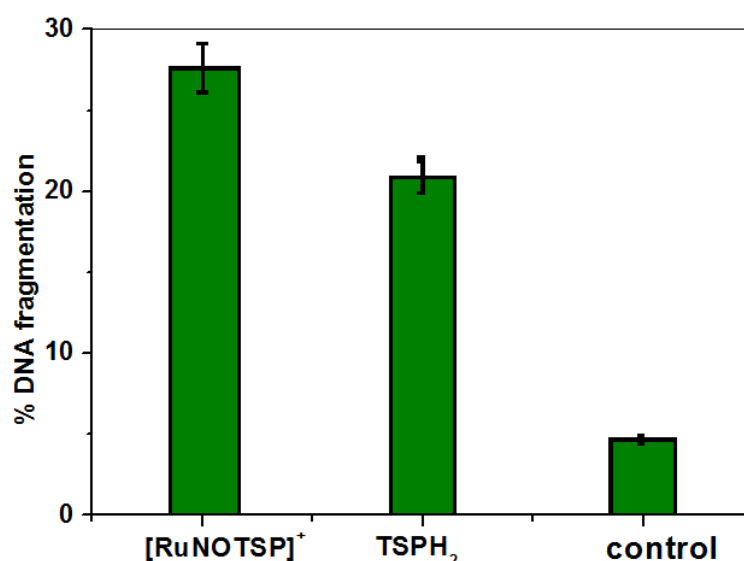


Figure 11. Plots of  $k_{\text{obs}}$  vs. concentration of [RuNOTSP]<sup>+</sup> and its ligand TSPH<sub>2</sub> in methanol.

Both  $k_{\text{on}}$  and  $k_{\text{off}}$  were used to obtain the equilibrium association constants ( $K_a$  [M<sup>-1</sup>] =  $k_{\text{on}}/k_{\text{off}}$ ) and the equilibrium dissociation constants ( $K_d$  [M] =  $k_{\text{off}}/k_{\text{on}}$ ). As shown in Figure 11, the  $k_{\text{obs}2}$  values for the second step were also found to increase with increasing [RuNOTSP]<sup>+</sup> and TSPH<sub>2</sub> concentration, although the increase was less compared to that of  $k_{\text{obs}1}$ . This is expected as the second step involves the compaction of the large CT-DNA molecule. [RuNOTSP]<sup>+</sup> binds to ctDNA with a second-order association constant of  $k_1 = 1.0 \pm 0.2 \text{ M}^{-1} \text{ s}^{-1}$  and dissociates from the binary complex with a first-order dissociation constant of  $k_{-1} = (4.1 \pm 0.1) \times 10^{-2} \text{ s}^{-1}$ , whereas TSPH<sub>2</sub> binds to CT-DNA with ( $k_1 = 0.7 \pm 0.1 \text{ M}^{-1} \text{ s}^{-1}$ ) and dissociates from the binary complex with ( $k_{-1} = (5.5 \pm 0.0) \times 10^{-2} \text{ s}^{-1}$ ). This means that the DNA binding affinity of [RuNOTSP]<sup>+</sup>,  $K_{a1}$ ,  $k_1/k_{-1}$  is much higher (45.6 M<sup>-1</sup>) than that of TSPH<sub>2</sub> (12.7 M<sup>-1</sup>) and that the equilibrium dissociation constant of [RuNOTSP]<sup>+</sup>,  $K_{d1}$ ,  $k_{-1}/k_1$  is  $2.2 \times 10^{-2} \text{ M}$ , which is much lower than TSPH<sub>2</sub> ( $7.9 \times 10^{-2} \text{ M}$ ). The presence of cationic [RuNOTSP]<sup>+</sup> in the negatively charged ctDNA solution facilitated a faster interaction, leading to a faster binding between the [RuNOTSP]<sup>+</sup> and ctDNA compared to the neutral TSPH<sub>2</sub>, and as a result, the formed ctDNA-[RuNOTSP]<sup>+</sup> is much more stable than ctDNA-TSPH<sub>2</sub>. The higher negative  $G_{\text{bind}}$  value of [RuNOTSP]<sup>+</sup> ( $-17.1 \text{ kJ mol}^{-1}$ ) compared to TSPH<sub>2</sub> ( $-6.7 \text{ kJ mol}^{-1}$ ) supports the higher stability of ctDNA-[RuNOTSP]<sup>+</sup> compared to ctDNA-TSPH<sub>2</sub>.

The data from the second reaction step, which included internal DNA rearrangement as well as electrostatic interaction and isomerization reaction, followed the same pattern as the first; a reversible reaction was observed for both [RuNOTSP]<sup>+</sup> and TSPH<sub>2</sub>. The





**Figure 12.** Plots of fragmented DNA quantification.

#### 2.4. Molecular Docking of DNA with [RuNOTSP]<sup>+</sup> and TSPH<sub>2</sub>

The molecular docking technique introduces a small molecule into the binding site of the DNA target-specific region primarily in a non-covalent mode, which can aid in rational drug design and mechanistic studies. Interaction mode and binding affinity docking studies on TSPH<sub>2</sub> and [RuNOTSP]<sup>+</sup> with B-DNA have been carried out to investigate the most likely binding site [70] (PDB ID: 1BNA). For molecular docking, we used the new server PatchDock [71], and the best docking model is shown in Figures 13 and 14. As the DNA fragment (2L8i) contains a triazole template, which has a far better affinity and specificity than unmodified oligonucleotides, and it is also highly resistant to nuclease destruction [72]. Both compounds [RuNOTSP]<sup>+</sup> and TSPH<sub>2</sub> are docked to the major groove of the DNA fragment (2L8i), as seen in (Figures 13 and 14), where [RuNOTSP]<sup>+</sup> binds to DNA through different types of interactions as one sulfur atom forms one hydrogen bond (HB) with strand B (SB), adenine Base Strand (A) (SA) Number 16; also one HB between oxygen and Cytosine (C) base SA No. 9; van der Waals interaction between [RuNOTSP]<sup>+</sup> and different bases such as C No. 12 SA, Guanine (G) No. 13 SA, C No. 17 SB, G No. 18 SB;  $\pi$ - $\pi$  stacking interaction between phenyl group and G No. 10 SA;  $\pi$ -sulfur stacking interaction with sulfur atom and Thymine (T) No. 11 SA; pi-anion interaction with G No. 15 SB and steric effect at nitrogen and C No. 14 SB. These different types of interaction for [RuNOTSP]<sup>+</sup> are stronger and more stable than TSPH<sub>2</sub>, as shown in (Figures 13 and 14). TSPH<sub>2</sub> binds to DNA by several types of interactions as two sulfur atoms forms: 2 HB with SB G Number 18; HB between sulfur and triazole linker No. 19 [73]; van der Waals interaction between TSPH<sub>2</sub> and different bases such as C No. 12 SA, T No. 11 SA, and T No. 20 SB; HB with nitrogen and G No. 10 SA;  $\pi$ -sulfur stacking interaction with sulfur atom and carbon of the TSPH<sub>2</sub> and steric effect at nitrogen and C No. 9 SA. The hydrogen bond acceptor sites of the DNA phosphate group in combination with DNA polymerase can thus be mimicked using the triazole template strand [53] or TSPH<sub>2</sub>, and this will have an effect on DNA bending, rigidity, and recognition. In a previous study [41], the docking results showed that BSA-[RuNOTSP]<sup>+</sup> with binding affinity (−7.27 kcal/mol) and BSA-TSPH<sub>2</sub> with binding affinity (−8.05 kcal/mol) are located in subdomain IA and it has recently been reported as a possible binding site for drugs on BSA [74].

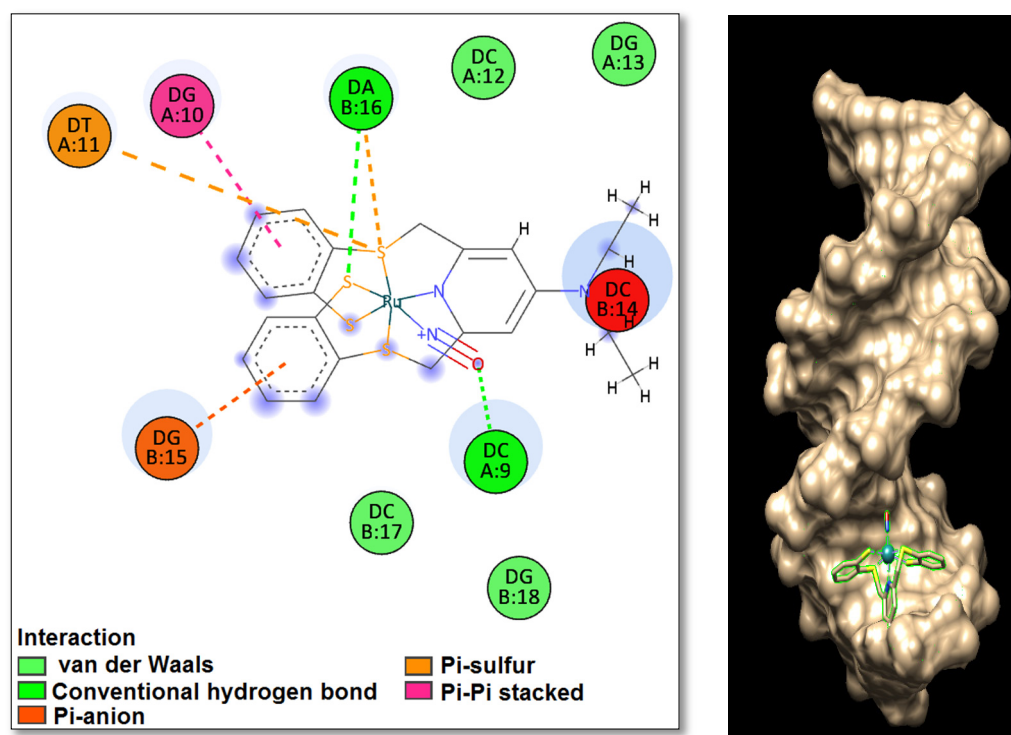


**Figure 13.** Different types of interactions between  $[\text{RuNOTSP}]^+$  and DNA bases as in the first view to the left while in the second view display  $[\text{RuNOTSP}]^+$  docked to the major groove of DNA fragment (2L8i).

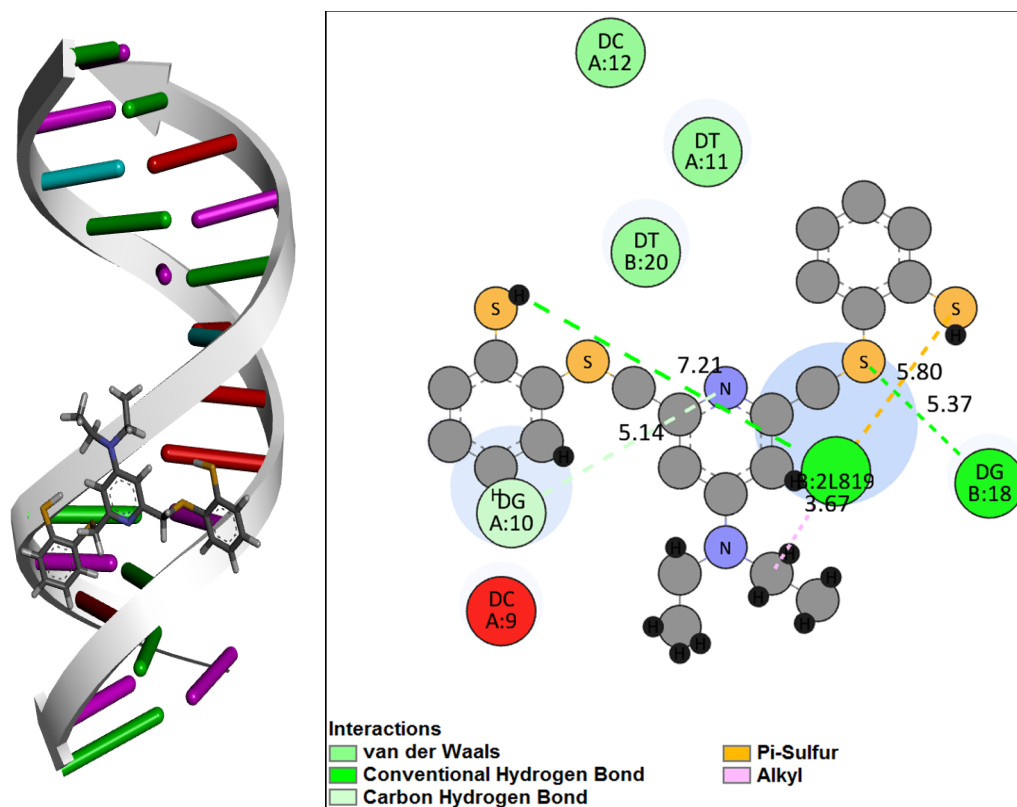


**Figure 14.**  $\text{TSPH}_2$  docked to major groove of DNA fragment (2L8i) as in the first view to the left while in the second view displays different types of interactions between  $\text{TSPH}_2$  and DNA bases.

### 3. Conclusions

In the current study, the interaction of DNA with [RuNOTSP]<sup>+</sup> and its ligand TSPH<sub>2</sub> is studied by fluorescence quenching, UV–vis absorption studies, stopped-flow, and molecular docking. The fluorescence enhancement spectra of both compounds are controlled by a static enhancement mechanism. The intrinsic binding constants ( $K_b$ ),  $(2.4 \pm 0.2) \times 10^5 \text{ M}^{-1}$  [RuNOTSP]<sup>+</sup> and  $(1.9 \pm 0.3) \times 10^5 \text{ M}^{-1}$  (TSPH<sub>2</sub>), as well as the enhancement dynamic constants ( $K_D$ ),  $(3.3 \pm 0.3) \times 10^4 \text{ M}^{-1}$  and  $(2.6 \pm 0.2) \times 10^4 \text{ M}^{-1}$  (TSPH<sub>2</sub>), reveal strong electrostatic binding via the phosphate backbone of the DNA helix. Stopped-flow experiments showed that both compounds bind through two reversible steps: a fast second-order binding, followed by a slow first-order isomerization reaction via a static quenching mechanism. The total binding constants for [RuNOTSP]<sup>+</sup> ( $K_a = 43.7 \text{ M}^{-1}$ ,  $K_d = 2.3 \times 10^{-2} \text{ M}^{-1}$ ,  $\Delta G^0 = -36.6 \text{ kJ mol}^{-1}$ ) and TSPH<sub>2</sub> ( $K_a = 15.1 \text{ M}^{-1}$ ,  $K_d = 66 \times 10^{-2} \text{ M}$ ,  $\Delta G^0 = -19 \text{ kJ mol}^{-1}$ ) revealed that the relative reactivity is approximately  $([\text{RuNOTSP}]^+)/(\text{TSPH}_2) = 3/1$ . The significantly negative  $\Delta G^0$  values are consistent with a spontaneous binding reaction to both [RuNOTSP]<sup>+</sup> and TSPH<sub>2</sub> with [RuNOTSP]<sup>+</sup> is very favorable. Cationic [RuNOTSP]<sup>+</sup> exhibited preferential efficient cleavage activity towards the minor groove of pBR322 DNA and via the hydrolytic pathway compared to TSPH<sub>2</sub>. The results revealed that the Ru(II) center was found to influence the rate but not the mechanism and showed that the [RuNOTSP]<sup>+</sup> complex is more prominent in DNA binders than the ligand TSP due to the strong electrostatic interaction of the [RuNOTSP]<sup>+</sup> cation towards the phosphate end of DNA. The optimized geometric structures of the ligand and its metal complexes are in good agreement with the experimental results. Molecular docking studies show that [RuNOTSP]<sup>+</sup> and TSPH<sub>2</sub> interact in a parallel manner with the major groove of the DNA backbone through non-covalent interactions such as hydrogen bonding, van der Waals, and hydrophobic interactions. The obtained data indicate that [RuNOTSP]<sup>+</sup> has a higher activity than TSPH<sub>2</sub>.

### 4. Experimental Section

#### 4.1. Materials

We prepared [RuNOTSP]<sup>+</sup> and TSPH<sub>2</sub>, and then used UV–vis, IR, electrical, and mass spectroscopy studies to characterize them. These outcomes have been compared with those from our studies that have been published [33]. The stock solutions ( $1 \times 10^{-3} \text{ M}$ ) of [RuNOTSP]<sup>+</sup> and TSPH<sub>2</sub> were prepared using methanol, which was then diluted to create working solutions for various spectroscopic techniques. Sigma (Saint Louis, MO, USA), provided the CT-DNA, which was then used without further purification. The stock solution of CT-DNA was made by dissolving a specific quantity of CT-DNA in Tris-HCl buffer at pH 7.2 and room temperature. The solution was then stored at 4 °C in the dark and used right away. With the aid of UV absorption and a molar extinction coefficient of ( $\epsilon$ ) equal to  $6600 \text{ M}^{-1} \text{ cm}^{-1}$  at 260 nm, its concentration was ascertained [75].

#### 4.2. Apparatus

A JASCO spectrophotometer (FP-8300) using quartz cuvettes of 1 cm was used to measure the absorption spectra of CT-DNA in the absence and presence of the current compounds with different concentrations of [RuNOTSP]<sup>+</sup> and TSPH<sub>2</sub>, which were recorded at 270–500 nm. Fluorescence measurements were carried out with a JASCO spectrofluorimeter (FP 6200) by keeping the concentration of RuNOTSP<sup>+</sup> and TSPH<sub>2</sub> constant ( $10^{-5} \text{ M}$ ) while varying the ctDNA concentration from 0 to  $1.5 \times 10^{-5} \text{ M}$ .

#### 4.3. Stopped-Flow Kinetic Studies

The kinetic measurements were carried out with the Applied KinetAsyst SF-61DX2 stopped-flow instrument (HI-Tech Scientific, Kolkata, West Bengal, India) and a Peltier thermostat. [RuNOTSP]<sup>+</sup> and TSPH<sub>2</sub> solutions were used at various concentrations. In the first step, solutions of DNA, and [RuNOTSP]<sup>+</sup> or TSPH<sub>2</sub> were added to each of the two syringes of the kinetic accessory. Then, equal volumes of both solutions were simultaneously injected into the sample chamber, and this process was repeated for each run.



The DNA's absorption spectra were continuously monitored before ( $t = 0$  s) and after the injection in the presence of  $[\text{RuNOTSP}]^+$  and  $\text{TSPH}_2$ . When the instrument's dead time was measured for a 1:1 mixture, it was found to be 2 ms. In control experiments, DNA solution was combined with buffer solutions devoid of  $[\text{RuNOTSP}]^+$  or  $\text{TSPH}_2$ . Decomposition of the DNA was ruled out because the absorption signal of the DNA did not change over the course of the control experiment. The complex nature of the kinetic trace indicated the presence of multiple steps, so we assumed a superposition of exponential terms to express the process (Equation (7)).

#### 4.4. *ctDNA Cleavage Activity*

Chemosensitivity testing involved the DNA fragmentation assay with diphenylamine [76]. In detail: Harvest monolayer cultures by scraping cells into the medium with a rubber policeman (or, for suspension cultures, directly into centrifuge tubes) and centrifuging ( $300\times g$ ) at  $4\text{ }^\circ\text{C}$  for 10 min to pellet the cells. The cell pellet was dissolved in 0.7 mL of ice-cold lysis buffer and 0.8 mL of 10 mM phosphate-buffered saline (PBS) with pH 7.4. The cell lysate was put into microfuge tubes and allowed to sit there for 15 min on ice. After 15 min at  $4\text{ }^\circ\text{C}$ , the  $13,000\times g$  lysate was centrifuged to separate high-molecular-weight DNA from DNA that had been broken up. The supernatant was transferred to a 5 mL glass tube (about 1.5 mL containing fragmented DNA). The intact DNA pellet was suspended in 1.5 mL of Tris-acetate-EDTA (TE) buffer before being transferred to another 5 mL glass tube. Each tube received 1.5 mL of 10% trichloroacetic acid (TCA), which was incubated for 10 min at room temperature and then centrifuged ( $500\times g$ ) at  $4\text{ }^\circ\text{C}$  for 15 min and the supernatant discarded. The 10% TCA precipitates were re-suspended in 0.7 mL of 5% TCA, boiled for 15 min at  $100\text{ }^\circ\text{C}$ , cooled to room temperature, and centrifuged ( $300\times g$ ) for 15 min at  $4\text{ }^\circ\text{C}$ . Without disturbing the precipitate, 0.5 mL of the supernatant was transferred to a fresh glass tube. After adding 1 mL of the diphenylamine reagent, the absorbance at 600 nm was measured after an overnight incubation at  $30\text{ }^\circ\text{C}$ . Percentage of DNA fragmentation was calculated as follows:

$$\text{DNA fragmentation (\%)} = \frac{\text{OD}_{600} \text{ of the supernatant}}{\text{OD}_{600} \text{ of the supernatant} + \text{OD}_{600} \text{ of the pellet}} \times 100 \quad (9)$$

#### 4.5. *Computational Studies*

The Gaussian 09 W package [77] was used to calculate quantum parameters using density functional theory (DFT) [78,79]. The singlet state of the complexes' molecular geometry was optimized at the B3LYP level of theory [80,81] using the basis set 6-31 g(d) for the ligand  $\text{TSPH}_2$  and LAN2DZ [49] for the metal in  $[\text{RuNOTSP}]^+$ . In the gas phase state, all calculations were optimized, and the optimized coordinates are listed in Supplementary Materials (Tables S2, S4 and S6). Frequency calculations for each optimized geometry were done at the same theoretical level to verify if the compound is a minimum or in the transition state. Natural population analysis (NPA) [43–45] was performed at B3LYP/6-311 G + (d,p.) using the NBO program version 3.1 [82] to calculate the atomic charge and their impact on the structure and stability of our systems, and the full data are listed in Tables S1, S3 and S5. The ChemCraft program was used to display the distribution of the highest occupied molecular orbital (HOMO), lowest unoccupied molecular orbital (LUMO), and frontier molecular orbital (FMO), which were calculated for  $\text{TSPH}_2$  and its complex [83]. The Gaussian view package was used to analyze the molecular electrostatic potential (MEP) [84].

#### 4.6. *Molecular Docking*

Density functional theory (DFT) B3LYP was used to optimize the structures of  $\text{TSPH}_2$  and  $[\text{RuNOTSP}]^+$ . The B-DNA crystal data (PDB 1D:1BNA) were obtained from the Protein Data Bank. A geometry-based molecular docking method PatchDock was used [71]. Its goal is to perform molecular docking procedures, which result in favorable complementarity

of molecular shapes. Such modifications lead to interface region interactions and minor steric conflicts when they are applied. A wide interface is produced as a result of the multiple complementary local features of the linked molecules that match each other. The Connolly dot surface representation of the molecules [85,86] is divided into concave, convex, and flat patches by the PatchDock method. Following that, complementary patches were matched to create candidate complexes. A scoring formula that takes into account both geometric fit and atomic desolvation energy was used to further assess each feasible change [87]. Finally, using root mean square deviation (RMSD), the candidate complexes were clustered to remove redundant structures. Due to the large part of PatchDock's quick transformational search, which relies on local feature matching rather than exhaustively searching the six-dimensional transformation space, it is highly efficient. By utilizing powerful data structures and spatial pattern recognition algorithms created in the field of computer vision, such as geometric hashing and posture clustering, and as described in the literature [88], it reduces computational processing time even further.

**Supplementary Materials:** The following supporting information can be downloaded at: <https://www.mdpi.com/article/10.3390/molecules28073028/s1>, Scheme S1: Synthetic route for [RuNOTSP]Br and its ligand TSPH<sub>2</sub>, respectively; Figure S1: Structure of TSPH<sub>2</sub>; Figure S2: Structure of TSP<sup>2-</sup>; Figure S3: Structure of [RuNOTSP]<sup>+</sup> cation; Table S1: Summary of Natural Population Analysis (NPA) of TSPH; Table S2: Coordinates parameters for TSPH<sub>2</sub>; Table S3: Summary of Natural Population Analysis (NPA) for TSP<sup>2-</sup> anion; Table S4: Coordinates parameters for TSP<sup>2-</sup> anion; Table S5: Summary of Natural Population Analysis (NPA) of [RuNOTSP]<sup>+</sup>; Table S6: Coordinates parameters for [RuNOTSP]<sup>+</sup> cation.

**Author Contributions:** H.A.S.: investigation, methodology, draft writing; S.Y.S.: project administration, supervision, revision; Y.S.M.: data curation, methodology, software, revision; F.I.E.: investigation, data curation; A.M.E.-N.: project administration, supervision; R.v.E.: project administration, revision. All authors have read and agreed to the published version of the manuscript.

**Funding:** This research received no external funding.

**Institutional Review Board Statement:** Not applicable.

**Informed Consent Statement:** Not applicable.

**Data Availability Statement:** Not applicable.

**Conflicts of Interest:** The authors declare no conflict of interest.

## References

1. Zhang, C.; Xu, C.; Gao, X.; Yao, Q. Platinum-based drugs for cancer therapy and anti-tumor Strategies. *Theranostics* **2022**, *12*, 2115–2132. [CrossRef]
2. Wheate, N.J.; Walker, S.; Craig, G.E.; Oun, R. The status of platinum anticancer drugs in the clinic and in clinical trials. *Dalton Trans.* **2010**, *39*, 8113–8127. [CrossRef]
3. Rottenberg, S.; Disler, C.; Perego, P. The rediscovery of platinum-based cancer therapy. *Nat. Rev. Cancer* **2020**, *21*, 37–50. [CrossRef]
4. Dasari, S.; Tchounwou, P.B. Cisplatin in cancer therapy: Molecular mechanisms of action. *Eur. J. Pharmacol.* **2014**, *740*, 364–378. [CrossRef]
5. Lee, S.Y.; Kim, C.Y.; Nam, T.-G. Ruthenium Complexes as Anticancer Agents: A Brief History and Perspectives. *Drug Des. Dev. Ther.* **2020**, *14*, 5375–5392. [CrossRef]
6. Fabijańska, M.; Kasprzak, M.M.; Ochocki, J. Ruthenium(II) and Platinum(II) Complexes with Biologically Active Aminoflavone Ligands Exhibit In Vitro Anticancer Activity. *Int. J. Mol. Sci.* **2021**, *22*, 7568. [CrossRef]
7. Sun, Q.; Li, Y.; Shi, H.; Wang, Y.; Zhang, J.; Zhang, Q. Ruthenium Complexes as Promising Candidates against Lung Cancer. *Molecules* **2021**, *26*, 4389. [CrossRef]
8. Kanaoujija, R.; Meenakshi; Srivastava, S.; Singh, R.; Mustafa, G. Recent advances and application of ruthenium complexes in tumor malignancy. *Mater. Today Proc.* **2023**, *72*, 2822–2827. [CrossRef]
9. Singha, A.K.; Pandey, D.S.; Xua, Q.; Braunstein, P. Recent advances in supramolecular and biological aspects of arene ruthenium (II) complexes. *Coord. Chem. Rev.* **2014**, *270*, 31–56. [CrossRef]
10. Bergamo, A.; Gaidon, C.; Schellens, J.H.M.; Beijnen, J.H.; Sava, G.J. Approaching tumour therapy beyond platinum drugs: Status of the art and perspectives of ruthenium drug candidates. *J. Inorg. Biochem.* **2012**, *106*, 90–99. [CrossRef]

11. Khamrang, T.; Kartikeyan, R.; Velusamy, M.; Rajendiran, V.; Dhivya, R.; Perumalsamy, B.; Akbarsha, M.A.; Palaniandavar, M. Synthesis, structures, and DNA and protein binding of ruthenium(ii)-p-cymene complexes of substituted pyridylimidazo[1,5-a]pyridine: Enhanced cytotoxicity of complexes of ligands appended with a carbazole moiety. *RSC Adv.* **2016**, *6*, 114143–114258. [[CrossRef](#)]
12. Hu, P.C.; Wang, Y.; Zhang, Y.; Song, H.; Gao, F.F.; Lin, H.Y.; Wang, Z.H.; Wei, L.; Yang, F. Novel mononuclear ruthenium(ii) complexes as potent and low-toxicity antitumour agents: Synthesis, characterization, biological evaluation and mechanism of action. *RSC Adv.* **2016**, *6*, 29963–29976. [[CrossRef](#)]
13. Kamatchi, T.S.; Kalaivani, P.F.; Fronczek, R.; Natarajan, K.; Prabhakaran, R. The effect of incorporating carboxylic acid functionalities into 2,2'-bipyridine on the biological activity of the complexes formed: Synthesis, structure, DNA/protein interaction, antioxidant activity and cytotoxicity. *RSC Adv.* **2017**, *7*, 46531–46547. [[CrossRef](#)]
14. Chen, L.M.; Peng, F.; Li, G.D.; Jie, X.M.; Cai, K.R.C.; Zhong, Y.; Zeng, H.; Li, W.; Zhang, Z.; Chen, J.C. The studies on the cytotoxicity in vitro, cellular uptake, cell cycle arrest and apoptosis-inducing properties of ruthenium methylimidazole complex [Ru(MeIm)<sub>4</sub>(p-cpip)](2+). *J. Inorg. Biochem.* **2016**, *156*, 64–74. [[CrossRef](#)]
15. Chen, W.X.; Song, X.D.; He, S.F.; Sun, J.; Chen, J.X.; Wu, T.; Mao, Z.W. Ru(II) complexes bearing guanidinium ligands as potent anticancer agents. *J. Inorg. Biochem.* **2016**, *164*, 91–98. [[CrossRef](#)]
16. Zhang, C.; Han, B.J.; Zeng, C.C.; Lai, S.H.; Li, W.; Tang, B.; Wan, D.; Jiang, G.B.; Liu, Y.J. Synthesis, characterization, in vitro cytotoxicity and anticancer effects of ruthenium (II) complexes on BEL-7402 cells. *J. Inorg. Biochem.* **2016**, *157*, 62–72. [[CrossRef](#)]
17. Süß-Fink, G. Areneruthenium complexes as anticancer agents. *Dalton Trans.* **2010**, *39*, 1673–1688. [[CrossRef](#)]
18. Bratsos, I.; Jedner, S.; Gianferrara, T.; Alessio, E. Ruthenium Anticancer Compounds: Challenges and Expectations. *Chimia* **2007**, *61*, 692–697. [[CrossRef](#)]
19. Meng, X.; Leyva, M.L.; Jenny, M.; Gross, I.; Benosman, S.; Fricker, B.; Harlepp, S.; Ebraud, P.H.; Boos, A.; Wlosik, P.; et al. A Ruthenium-Containing Organometallic Compound Reduces Tumor Growth through Induction of the Endoplasmic Reticulum Stress Gene CHOP. *Cancer Res.* **2009**, *69*, 5458–5466. [[CrossRef](#)]
20. Gupta, G.; Nowak-Sliwinska, P.; Dyson, N.P.J.; Therrien, B. Increasing the selectivity of biologically active tetranuclear arene ruthenium assemblies. *Inorg. Chim. Acta* **2014**, *423*, 524–529. [[CrossRef](#)]
21. Sava, G.; Bergamo, A.; Dyson, P.J. Metal-based antitumour drugs in the post-genomic era: What comes next? *Dalton Trans.* **2011**, *40*, 9069–9075. [[CrossRef](#)]
22. Hartinger, C.G.; Metzler-Nolte, N.; Dyson, P.J. Challenges and Opportunities in the Development of Organometallic Anticancer Drugs. *Organometallics* **2012**, *31*, 5677–5685. [[CrossRef](#)]
23. Kilpin, K.J.; Crot, S.; Riedel, T.; Kitchen, J.A.; Dyson, P.J. Ruthenium(ii) and osmium(ii) 1,2,3-triazolylidene organometallics: A preliminary investigation into the biological activity of 'click' carbene complexes. *Dalton Trans.* **2014**, *43*, 1443–1448. [[CrossRef](#)]
24. Stepanenko, I.; Zalibera, M.; Schaniel, D.; Telser, J.; Arion, V.B. Ruthenium-nitrosyl complexes as NO-releasing molecules, potential anticancer drugs, and photoswitches based on linkage isomerism. *Dalton Trans.* **2022**, *51*, 5367–5393. [[CrossRef](#)]
25. Gallo, O.; Masini, E.; Morbidelli, L.; Franchi, A.; Fini-Storchi, I.; Vergari, W.A.; Ziche, M. Role of nitric oxide in angiogenesis and tumor progression in head and neck cancer. *J. Natl. Cancer Inst.* **1998**, *90*, 587–596. [[CrossRef](#)]
26. Ziche, M.; Morbidelli, L. Nitric oxide and angiogenesis. *J. Neurooncol.* **2000**, *50*, 139–148. [[CrossRef](#)]
27. Gomes, M.G.; Davanzo, C.U.; Silva, S.C.; Lopes, L.G.F.; Santos, P.S.; Franco, D.W. Cis- and trans-nitrosyltetraammineruthenium(II). Spectral and electrochemical properties and reactivity. *J. Chem. Soc. Dalton Trans.* **1998**, 601–608. [[CrossRef](#)]
28. Enemark, J.H.; Feltham, R.D. Principles of structure, bonding, and reactivity for metal nitrosyl complexes. *Coord. Chem. Rev.* **1974**, *13*, 339–406. [[CrossRef](#)]
29. Wolak, M.; van Eldik, R. To be or not to be NO in coordination chemistry? A mechanistic approach. *Coord. Chem. Rev.* **2002**, *230*, 263–282. [[CrossRef](#)]
30. Karidi, K.; Garoufis, A.; Tshipis, A.; Hadjiliadis, N.; den Dulk, H.; Reedijk, J. Synthesis, characterization, in vitro antitumor activity, DNA-binding properties and electronic structure (DFT) of the new complex cis-(Cl,Cl)[RuII(Cl<sub>2</sub>(NO<sup>+</sup>)(terpy)]Cl. *Dalton Trans.* **2005**, 1176–1187. [[CrossRef](#)]
31. Sellmann, D.; Shaban, S.Y.; Heinemann, F.W. Syntheses, Structures and Reactivity of Electron-Rich Fe and Ru Complexes with the New Pentadentate Ligand Et<sub>2</sub>NpyS<sub>4</sub>-H<sub>2</sub> {4-(Diethylamino)2,6-bis[(2-mercaptophenyl) thiomethyl] pyridine}. *Eur. J. Inorg. Chem.* **2004**, *23*, 4591–4601. [[CrossRef](#)]
32. Sellmann, D.; Binder, H.; Häußinger, D.; Heinemann, F.W.; Sutter, J. Transition metal complexes with sulfur ligands: Part CXLIV. Square planar nickel complexes with NiS<sub>4</sub> cores in three different oxidation states: Synthesis, X-ray structural and spectroscopic studies. *Inorg. Chim. Acta* **2000**, *300*, 829–836. [[CrossRef](#)]
33. Sellmann, D.; Gottschalk-Gaudig, T.; Haussinger, D.; Heinemann, F.W.; Hess, B.A. Ru(HNO)(<sup>+</sup>pybuS<sub>4</sub><sup>+</sup>), the First HNO Complex Resulting from Hydride Addition to a NO Complex (<sup>+</sup>pybuS<sub>4</sub><sup>2+</sup>-2,6-Bis(2-mercapto-3,5-di-tert-butylphenylthio)dimethylpyridine(2-)). *Chem. Eur. J.* **2001**, *7*, 1874–1880. [[CrossRef](#)]
34. Prakash, R.; Czaja, A.U.; Heinemann, F.W.; Sellmann, D. Visible Light Induced Reversible Extrusion of Nitric Oxide from a Ruthenium(II) Nitrosyl Complex: A Facile Delivery of Nitric Oxide. *J. Am. Chem. Soc.* **2005**, *127*, 13758–13759. [[CrossRef](#)]
35. Dias, R.S.; Lindman, B. *DNA Interactions with Polymers and Surfactants*; Wiley and Sons: Hoboken, NJ, USA, 2008; pp. 1–432.
36. Martinez, R.; Chacn-Garca, L. The search of DNA-intercalators as antitumoral drugs: What it worked and what did not work. *Curr. Med. Chem.* **2005**, *12*, 127–151. [[CrossRef](#)]

37. Shereef, H.A.; Shaban, S.Y.; Moemen, Y.S.; El-Khouly, M.E.; El-Nahas, A.M. Biophysicochemical studies of a ruthenium(II) nitrosyl thioether-thiolate complex binding to BSA: Mechanistic information, molecular docking, and relationship to antibacterial and cytotoxic activities. *Appl. Organomet. Chem.* **2022**, *34*, e6583. [[CrossRef](#)]
38. Shaban, N.Z.; Aboelsaad, A.M.; Shoueir, K.R.; Abdulmalek, S.A.; Awad, D.; Shaban, S.Y.; Mansour, H. Chitosan-based dithiophenolato nanoparticles: Preparation, mechanistic information of DNA binding, antibacterial and cytotoxic activities. *J. Mol. Liq.* **2020**, *318*, 114252. [[CrossRef](#)]
39. Elshami, F.I.; Ramadan, A.E.M.M.; Ibrahim, M.M.; El-Mehasseb, I.M.; Al-Juaid, S.; Shaban, S.Y. Metformin Containing Nickel (II) Complexes: Synthesis, Structural Characterization, Binding and Kinetic Interactions with BSA, Antibacterial and in-vitro Cytotoxicity Studies. *Appl. Organomet. Chem.* **2020**, *34*, e5437. [[CrossRef](#)]
40. Shaban, N.Z.; Yehia, S.A.; Shoueir, K.R.; Saleh, S.R.; Awad, D.; Shaban, S.Y. Design, DNA binding and kinetic studies, antibacterial and cytotoxic activities of stable dithiophenolato titanium(IV)-chitosan Nanocomposite. *J. Mol. Liq.* **2019**, *287*, 111002. [[CrossRef](#)]
41. Ramzy, E.; Ibrahim, M.M.; El-Mehasseb, I.M.; Ramadan, A.E.M.M.; Elshami, F.I.; Shaban, Y.S.; van Eldik, R. Synthesis, Biophysical Interaction of DNA/BSA, Equilibrium and Stopped-Flow Kinetic Studies, and Biological Evaluation of bis(2-Picolyl)amine-Based Nickel(II) Complex. *Biomimetics* **2022**, *7*, 172. [[CrossRef](#)]
42. Sellmann, D.; Engel, K.; Heinemann, F.W. Inert and Labile [Ru(L)(‘pyS4’)] Complexes with Rigid [RuNS4] Cores and trans-Thiolate Donors [L = PPh<sub>3</sub>, PEt<sub>3</sub>, DMSO, CO, NO<sup>+</sup>, N<sub>2</sub>H<sub>4</sub>; ‘pyS4’<sup>2-</sup> = 2,6-Bis(2-mercaptophenylthio)dimethylpyridine(2-)]. *Eur. J. Inorg. Chem.* **2000**, *3*, 423–429. [[CrossRef](#)]
43. Reed, A.E.; Weinstock, R.B.; Weinhold, F.J. Natural population analysis. *Chem. Phys.* **1985**, *83*, 735. [[CrossRef](#)]
44. Reed, A.; Curtiss, L.A.; Weinhold, F. Intermolecular interactions from a natural bond orbital, donor-acceptor viewpoint. *Chem. Rev.* **1988**, *88*, 899. [[CrossRef](#)]
45. Kwon, O.; Sevin, F.; McKee, M.L. Density Functional Calculations of Methylolithium, t-Butyllithium, and Phenyllithium Oligomers: Effect of Hyperconjugation on Conformation. *J. Phys. Chem. A* **2001**, *105*, 913–922. [[CrossRef](#)]
46. Masoud, M.S.; Ali, A.E.; Shaker, M.A.; Elsalal, G.S. Synthesis, computational, spectroscopic, thermal and antimicrobial activity studies on some metal-urate complexes. *Spectrochim. Acta A* **2012**, *90*, 93–108. [[CrossRef](#)]
47. Zhao, C.; Lin, H.; Zhu, S.; Sun, H.; Chen, Y. Dinuclear palladium (II) complexes containing two monofunctional [Pd(en)(pyridine)Cl]<sup>+</sup> units bridged by Se or S. Synthesis, characterization, cytotoxicity and kinetic studies of DNA-binding. *J. Inorg. Biochem.* **1998**, *70*, 219–226. [[CrossRef](#)]
48. Lwebuga-Mukasa, J.S.; Harper, E. Taylor Palmer. Collagenase enzymes from Clostridium: Characterization of individual enzymes. *Biochemistry* **1976**, *15*, 4736–4741.
49. Tabassum, S.; Zaki, M.; Arjmand, F.; Ahmad, I. Synthesis of heterobimetallic complexes: In vitro DNA binding, cleavage and antimicrobial studies. *J. Photochem. Photobiol. B. Biol.* **2012**, *114*, 108–118. [[CrossRef](#)]
50. Tabassum, S.; Parveen, M.; Ali, A.; Alam, M.; Ahmad, A.; Khan, A.U.; Khan, R.A. Synthesis of Aryl-1, 2, 4, 5-tetrazinane-3-thiones, in vitro DNA binding studies, nuclease activity and its antimicrobial activity. *J. Mol. Struct.* **2012**, *1020*, 33–40. [[CrossRef](#)]
51. Ahmedi, F.; Alizadeh, A.A.; Shahabadi, N.; Rhimi-Nasrabi, M. Study bonding of Al-Curcumin complex to ds-DNA, monitoring by multispectroscopic and voltammetric techniques. *Spectrochim. Acta A Mol. Biomol. Spectrosc.* **2011**, *79*, 1466–1474, Erratum in *Spectrochim. Acta A Mol. Biomol. Spectrosc.* **2012**, *90*, 230. [[CrossRef](#)]
52. Shahabadi, N.; Mohamedi, S. Synthesis Characterization and DNA Interaction Studies of a New Zn(II) Complex Containing Different Dinitrogen Aromatic Ligands. *Bioinorg. Chem. Appl.* **2012**, *2012*, 571913. [[CrossRef](#)] [[PubMed](#)]
53. Li, Y.; Korolev, S.; Waksman, G. Crystal structures of open and closed forms of binary and ternary complexes of the large fragment of Thermus aquaticus DNA polymerase I: Structural basis for nucleotide incorporation. *EMBO J.* **1998**, *17*, 7514–7525. [[CrossRef](#)] [[PubMed](#)]
54. Shahabadi, N.; Fatahi, A. Multispectroscopic DNA binding studies of a tris-chelate nickel(II) complex containing 4,7-diphenyl 1,10-phenanthroline ligands. *J. Mol. Struct.* **2010**, *970*, 90–95. [[CrossRef](#)]
55. Barton, J.K.; Danishefsky, A.T.; Goldberg, J.M. Tris(phenanthroline) ruthenium (II): Stereoselectivity in binding to DNA. *J. Am. Chem. Soc.* **1984**, *106*, 2172–2176. [[CrossRef](#)]
56. Liu, X.W.; Li, J.; Deng, H.; Zheng, K.C.; Mao, Z.W.; Ji, L.N. Experimental and DFT studies on the DNA-binding trend and spectral properties of complexes [Ru(bpy)<sub>2</sub>L]<sup>2+</sup> (L = dmdpq, dpq, and dcdpq). *Inorg. Chim. Acta* **2005**, *358*, 3311–3319. [[CrossRef](#)]
57. Liu, X.W.; Li, J.; Li, H.; Zheng, K.C.; Chao, H.; Ji, L.N. Synthesis, characterization, DNA-binding and photocleavage of complexes [Ru(phen)<sub>2</sub>(6-OH-dppz)]<sup>2+</sup> and [Ru(phen)<sub>2</sub>(6-NO<sub>2</sub>-dppz)]<sup>2+</sup>. *J. Inorg. Biochem.* **2005**, *99*, 2372–2380. [[CrossRef](#)] [[PubMed](#)]
58. Barton, J.K.; Basil, L.A. A cobalt derivative of the restriction enzyme EcoRI. *Inorg. Chim. Acta* **1983**, *79*, 152–153. [[CrossRef](#)]
59. Benesi, H.A.; Hildebrand, J.A. Spectrophotometric Investigation of the Interaction of Iodine with Aromatic Hydrocarbons. *J. Am. Chem. Soc.* **1949**, *71*, 2703–2707. [[CrossRef](#)]
60. Kennedy, S.D.; Bryant, R.G. Manganese-deoxyribonucleic acid binding modes. Nuclear magnetic relaxation dispersion results. *Biophys. J.* **1986**, *50*, 669–676. [[CrossRef](#)] [[PubMed](#)]
61. Satyanarayana, S.; Dabrowiak, J.C.; Chaires, J.B. Neither delta- nor lambda tris(phenanthroline)ruthenium(II) binds to DNA by classical intercalation. *Biochemistry* **1992**, *31*, 9319–9324. [[CrossRef](#)] [[PubMed](#)]
62. Dey, D.; Maiti, C.; Maitib, S.; Dhara, D. Interaction between calf thymus DNA and cationic bottle-brush copolymers: Equilibrium and stopped-flow kinetic studies. *Phys.Chem.Chem.Phys.* **2015**, *17*, 2366–2377. [[CrossRef](#)] [[PubMed](#)]
63. Ilarduya, C.T.D.; Sun, Y.; Duezguenes, N. Gene Delivery by Lipoplexes and Polyplexes. *Eur. J. Pharm. Sci.* **2010**, *40*, 159–170.

64. Godbey, W.T.; Mikos, A.G. Recent Progress in Gene Delivery Using Non-viral Transfer Complexes. *J. Control. Release* **2001**, *72*, 115–125. [[CrossRef](#)]
65. Barreleiro, P.C.A.; Lindman, B. The Kinetics of DNA Cationic Vesicle Complex Formation. *J. Phys. Chem. B* **2003**, *107*, 6208–6213. [[CrossRef](#)]
66. Dey, D.; Kumar, S.; Maiti, S.; Dhara, D. Stopped-Flow Kinetic Studies of Poly(amidoamine) Dendrimers-Calf Thymus DNA to Form Dendriplexes. *J. Phys. Chem. B* **2013**, *117*, 13767–13774. [[CrossRef](#)] [[PubMed](#)]
67. Santhiya, D.; Dias, R.S.; Dutta, S.; Das, P.K.; Miguel, M.G.; Lindman, B.; Maiti, S. Kinetic Studies of Amino Acid- Based Surfactant Binding to DNA. *J. Phys. Chem. B* **2012**, *116*, 5831–5837. [[CrossRef](#)] [[PubMed](#)]
68. Li, D.-D.; Tian, J.-L.; Gu, W.; Liu, X.; Yan, S.-P. Synthesis X-ray crystal structures DNA binding and nuclease activities of two novel 124-triazole-based CuII complexes. *Eur. J. Inorg. Chem.* **2009**, *2009*, 5036–5045. [[CrossRef](#)]
69. Hu, X.; Luo, Q.; Qin, Y.; Wu, Y.; Liu, X.-W. DNA Interaction, DNA Photocleavage, Photocytotoxicity In Vitro, and Molecular Docking of Naphthyl-Appended Ruthenium Complexes. *Molecules* **2022**, *27*, 3676. [[CrossRef](#)] [[PubMed](#)]
70. Tang, B.; Shen, F.; Wan, D.; Guo, B.-H.; Wang, Y.-J.; Yia, Q.-Y.; Liu, Y.-J. DNA-binding, molecular docking studies and biological activity studies of ruthenium(II) polypyridyl complexes. *RSC Adv.* **2017**, *7*, 34945–34958. [[CrossRef](#)]
71. Schneidman-Duhovny, D.; Inbar, Y.; Nussinov, R.; Wolfson, H.J. PatchDock and SymmDock: Servers for rigid and symmetric docking. *Nucl. Acids. Res.* **2005**, *33*, W363–W367. [[CrossRef](#)] [[PubMed](#)]
72. Kumar, P.; Truong, L.; Baker, Y.R.; El-Sagheer, A.H.; Brown, T. Synthesis, Affinity for Complementary RNA and DNA, and Enzymatic Stability of Triazole-Linked Locked Nucleic Acids (t-LNAs). *ACS Omega* **2018**, *3*, 6976–6987. [[CrossRef](#)] [[PubMed](#)]
73. Dallmann, A.; El-Sagheer, A.H.; Dehmel, L.; Mügge, C.; Griesinger, C.N.; Ernsting, P.; Brown, T. Structure and Dynamics of Triazole-Linked DNA: Biocompatibility Explained. *Chem. Eur. J.* **2011**, *17*, 14714–14717. [[CrossRef](#)] [[PubMed](#)]
74. Siddiqui, S.; Mujeeb, A.; Ameen, F.; Mubarak-Ishqi, H.; Ur-Rehman, S.; Tabish, M. Investigating the mechanism of binding of nalidixic acid with deoxyribonucleic acid and serum albumin: A biophysical and molecular docking approaches. *J. Biomol. Struct. Dyn.* **2020**, *39*, 570–585. [[CrossRef](#)] [[PubMed](#)]
75. Reichmann, M.E.; Rice, S.A.; Thomas, C.A.; Doty, P. A Further Examination of the Molecular Weight and Size of Deoxypentose Nucleic Acid. *J. Am. Chem. Soc.* **1954**, *76*, 3047–3053. [[CrossRef](#)]
76. Blumenthal, R.D. (Ed.) *Methods in Molecular Medicine, Volume 111: Chemosensitivity: Volume 2: In Vivo Models, Imaging, and Molecular Regulators*; Humana Press Inc.: Totowa, NJ, USA, 2005.
77. Frisch, M.J.; Trucks, G.W.; Schlegel, H.B.; Scuseria, G.E.; Robb, M.A.; Cheeseman, J.R.; Scalmani, G.; Barone, V.; Mennucci, B.; Petersson, G.A.; et al. *Gaussian 09, Revision A.02*; Gaussian, Inc.: Wallingford, CT, USA, 2009.
78. Parr, R.G.; Yang, W. Density-functional theory of atoms and molecules. *Int. J. Quantum Chem.* **1993**, *47*, 101.
79. Ziegler, T. Approximate density functional theory as a practical tool in molecular energetics and dynamics. *Chem. Rev.* **1991**, *91*, 651–667. [[CrossRef](#)]
80. Becke, A.D. Density-functional thermochemistry. III. The role of exact exchange. *J. Chem. Phys.* **1993**, *98*, 5648–5652. [[CrossRef](#)]
81. Stephens, P.J.; Devlin, F.J.; Chabalowski, C.F.; Frisch, M.J. Ab Initio Calculation of Vibrational Absorption and Circular Dichroism Spectra Using Density Functional Force Fields. *J. Phys. Chem.* **1994**, *98*, 11623–11627. [[CrossRef](#)]
82. Lu, T.; Chen, F. Multiwfn: A multifunctional wavefunction analyzer. *J. Comput. Chem.* **2012**, *33*, 580–592. [[CrossRef](#)]
83. Zhurko, G.A.; Zhurko, D.A. Chemcraft. Version 1.7 (Build 132). Available online: [www.chemcraftprog.com](http://www.chemcraftprog.com) (accessed on 16 January 2023).
84. Hay, P.J.; Wadt, W.R. Ab initio effective core potentials for molecular calculations. Potentials for the transition metal atoms Sc to Hg. *J. Chem. Phys.* **1985**, *82*, 270. [[CrossRef](#)]
85. Connolly, M.L. Solvent-accessible surfaces of proteins and nucleic acids. *Science* **1983**, *221*, 709–713. [[CrossRef](#)] [[PubMed](#)]
86. Connolly, M.L. Analytical molecular surface calculation. *J. Appl. Crystallogr.* **1983**, *16*, 548–558. [[CrossRef](#)]
87. Zhang, C.; Vasmatzis, G.; Cornette, J.L.; DeLisi, C. Determination of atomic desolvation energies from the structures of crystallized proteins. *J. Mol. Biol.* **1997**, *267*, 707–726. [[CrossRef](#)]
88. Duhovny, D.; Nussinov, R.; Wolfson, H.J. Efficient Unbound Docking of Rigid Molecules. *Algorithms Mol. Biol.* **2002**, *2452*, 185–200.

**Disclaimer/Publisher’s Note:** The statements, opinions and data contained in all publications are solely those of the individual author(s) and contributor(s) and not of MDPI and/or the editor(s). MDPI and/or the editor(s) disclaim responsibility for any injury to people or property resulting from any ideas, methods, instructions or products referred to in the content.